Intermittent criticality multi-scale processes leading to large slip events on rough laboratory faults

Grzegorz Kwiatek[1], Patricia Martínez-Garzón[1], Thomas Goebel[2], Marco Bohnhoff[1,3], Yehuda Ben-Zion[4], Georg Dresen[1,5]

1. Helmholtz Centre Potsdam, GFZ German Research Centre for Geosciences, Section 4.2 Geomechanics and Scientific Drilling, Telegrafenberg, 14473 Potsdam, Germany
2. Department of Earth Sciences, Memphis Center for Earthquake Research and Information, University of Memphis, Memphis, United States.
3. Free University Berlin, Institute of Geological Sciences, Berlin, Germany
4. Department of Earth Sciences, University of Southern California and StatewideCalifornia Earthquake Center, Los Angeles, CA 90089-0740, United States.
5. Institute of Earth and Environmental Sciences, University of Potsdam, Potsdam, Germany.

Corresponding Author:

Grzegorz Kwiatek, Helmholtz Centre Potsdam, GFZ German Research Centre for Geosciences, Section 4.2 Geomechanics and Scientific Drilling, Telegrafenberg, 14473 Potsdam, Germany, email: kwiatek@gfz-potsdam.de

Key points:

We study preparatory processes preceding large slip events on rough laboratory faults using seismo-mechanical features derived from AE data

The analysis highlights multi-scale rapidly evolving damage, roughness and stress changes along the fault surface

Intermittent criticality marked by evolving stress correlations on different length scales can explain the observed patterns leading to large labquakes

Abstract

We discuss data of three laboratory stick-slip experiments on Westerly Granite samples performed at elevated confining pressure and constant displacement rate on rough fracture surfaces. The experiments produced complex slip patterns including fast and slow ruptures with large and small fault slips, as well as failure events on the fault surface producing acoustic emission bursts without externally-detectable stress drop. Preparatory processes leading to large slips were tracked with an ensemble of ten seismo-mechanical and statistical parameters characterizing local and global damage and stress evolution, localization and clustering processes, as well as event interactions. We decompose complex spatio-temporal trends in the lab-quake characteristics and identify persistent effects of evolving fault roughness and damage at different length scales, and local stress evolution approaching large events. The observed trends highlight labquake localization processes on different spatial and temporal scales. The preparatory process of large slip events includes smaller events marked by confined bursts of AE activity that collectively prepare the fault surface for a system-wide failure by conditioning the large-scale stress field. Our results are consistent overall with an evolving process of intermittent criticality leading to large failure events, and may contribute to improved forecasting of large natural earthquakes.

Plain language summary

We discuss failure events in laboratory experiments on a rough fault performed at pressures existing in the Earth's crust. The laboratory faults were subjected to constant displacement resulting in short-lasting slips of their fault surface. We observe complex slip patterns including fast/slow ruptures with large/small fault slips. Very small slips on the fault surface were observed only with acoustic emission (AE) activity, representing tiny earthquakes of sub-mm size that produce elastic waveforms that can be recorded with piezo sensors. Using parameters derived from AE data, we analyzed physical processes leading to large slip events of the lab fault surface, an equivalent of a large earthquake in nature. Our parameters characterize local and global damage, stress, as well as interactions of small fractures before the labquake. We identify evolving fault roughness at different length scales, and find that the preparatory processes preceding lab quakes are facilitated by small earthquakes marked with bursts of AE activity. These bursts indicate ruptures of individual fault patches, which then interact and collectively prepare the fault surface for the labquake. Our results provide a set of physics-based parameters describing complex processes leading to lab slip events that may allow to improve earthquake forecasting along natural faults.

1 Introduction

Fault processes leading to large earthquakes have occasionally been observed to produce foreshock activity and aseismic transients, sometimes lasting months or even years prior to the main shock (Kato et al., 2012; Bouchon et al., 2013; Schurr et al., 2014; Durand et al., 2020; Meng and Fan, 2021; Kwiatek et al., 2023). Seismic and aseismic precursors signifying fault damage evolution and progressive localization towards large dynamic ruptures are not well understood due to limited availability and resolution of seismic data and widely varying structures and properties of fault zones (e.g., Ben-Zion, 2008, and references therein). The role of precursory observables during the preparatory process before earthquakes and their potential use for forecasting remain controversial (Geller et al., 1997; Bakun et al., 2005; Ogata and Katsura, 2012; Wu et al., 2013; Mignan, 2014). Existing physical models describing the preparation and nucleation process on large pre-existing faults motivated by field and laboratory studies (Dieterich, 1978; Ohnaka, 1992; Ellsworth and Beroza, 1995; McLaskey, 2019; Kato and Ben-Zion, 2021) converge towards a combination of processes including accelerating preslip and, in some cases, cascading foreshocks. However, fault heterogeneity and structural variability of fault zones result in rich and varying observational phenomena, that often defy clear interpretation. Thus, seismic hazard assessment and earthquake forecasting still largely rely on probabilistic approaches (Ogata, 1999; Lippiello et al., 2019; Hirose et al., 2021; Mizrahi et al., 2023). The observation of a plethora of physical preparatory processes requires high-resolution monitoring of both seismic and aseismic failures using frequency bands that are hardly achievable in nature.

Laboratory experiments performed on intact and faulted rock samples with varying loading conditions have provided a wealth of observations characterizing the effects of roughness, gouge material, loading rate, effective normal stress, and stiffness ratio of the fault and loading system on long-term deformation leading to failure (Latour et al., 2013; Mclaskey and Yamashita, 2017; Leeman et al., 2018; Guérin-Marthe et al., 2019; Scuderi et al., 2020; Gounon et al., 2022; Morad et al., 2022). Motivated by experimental results, various studies (Ohnaka, 1992; Dieterich and Kilgore, 1996; Ben-Zion and Rice, 1997; Ohnaka and Shen, 1999; Latour et al., 2013) have suggested to separate the preparatory phase into a quasi-static phase and an accelerating phase producing dynamic slip (e.g. Okubo and Dietrich, 1984). This transition is often only loosely defined by the onset of a local or system-wide decrease in shear stress leading to an abrupt stress drop or transition in rupture velocity, and an overall change of energy flux into the rupture front tip. In a complex and heterogeneous fault zone, the preparation phase may be long-lasting. The transition towards nucleation of a large rupture involves a localization process, distributed creep transients and

89 collective failure of a range of asperities (de Geus et al., 2019; Lebihain et al., 2021; Yamashita et al.,
90 2021; McBeck et al., 2022). These processes lead to redistribution of stresses along the fault zone at
91 different length scales, reflecting the multi-scale evolution of roughness at the level of granular
92 material forming the fault zone, cm-scale asperities and large-scale structural inhomogeneities.

93 These multi-scale preparatory processes before large laboratory slip events are typically
94 accompanied by Acoustic Emission (AE) activity that allows monitoring key seismo-mechanical
95 processes and local stress evolution during the deformation cycle. Parameters derived from AE data
96 showed changes in clustering and localization of AE hypocenters, AE magnitude-frequency
97 distributions, ultrasonic velocities, inter-event triggering and other statistical attributes approaching
98 failure (Bolton et al., 2023; Main, 1991, 1992; Lockner, 1993; Zang et al., 1998; Goebel et al., 2012,
99 2013, 2014; Kwiatek et al., 2014b; Davidsen et al., 2017, 2017, 2021; Scuderi et al., 2017). Typically,
100 AE-derived parameters from stick-slip cycles exhibit general trends, which are punctuated and
101 partially reversed by large failure events. Although the observed trends for some parameters during
102 the preparatory slip indicate progressive damage and localization, estimating time-to-failure is still
103 challenging.

104 Forecasting the origin time of future large earthquakes remains a challenge if not an impossible task.
105 In recent years, earthquake forecasting made a leap using new opportunities provided by Artificial
106 Intelligence (AI) techniques. These techniques demonstrated an ability to predict time-to-failure in
107 direct shear laboratory tests on smooth faults (Johnson et al., 2021), as well as on analog models,
108 natural and induced seismicity, and synthetic modeling (e.g. Corbi et al., 2019; Johnson et al., 2021;
109 McBeck et al., 2021). Such studies use a number of potential precursory parameters derived from
110 seismic waveforms or earthquake catalogs (see e.g. Rouet-Leduc et al., 2017; Lubbers et al., 2018;
111 Hulbert et al., 2019; Picozzi and Iaccarino, 2021). Johnson et al. (2021) noted that successful cross-
112 scale earthquake forecasting requires generalization of predictive models and a better physical
113 understanding of input and output parameters. The former involves extension of the predictive AI-
114 aided modeling to studies of rough faults, whereas the latter requires a clear linking of AE-derived
115 precursory parameters with observable damage and stress evolution on different spatio-temporal
116 scales.

117 In this study we employ large AE datasets from laboratory stick-slip experiments involving a series of
118 tests performed on rough pre-fractured faults (e.g. Goebel et al., 2012;2013; 2014). The experiments
119 produced complex slip patterns including large and small slips of the fault surface (characterized by
120 large and small stress drops), and confined slips (with stress drops not measurable with the internal
121 load cell) accompanied by AE data bursts. The multi-scale preparatory processes preceding system-

wide slip events are analyzed with a set of physics-motivated AE-based features characterizing the seismo-mechanical spatio-temporal processes occurring on the fault. These include parameters describing damage and stress evolution, localization and clustering, event interactions, and local micromechanics and stress heterogeneity. We decompose the observed trends and discuss them in the context of roughness evolution at different spatial scales, a crossplay of local and global damage, and multi-scale stress evolution when approaching a system-size event.

2 Data and methods

2.1 Experimental setup and acoustic emission monitoring

Three triaxial stick-slip tests WgN04, WgN05 and WgN07 were conducted on cylindrical samples of Westerly Granite with dimensions of 40 mm diameter × 107 mm length (Goebel et al., 2012, 2013, 2014, 2015). Samples were prepared with a 2.5 cm deep notch inclined at 30° to the cylinder axis to guide formation of a shear fracture. The samples were first oven-dried at 100°C and subsequently encapsulated in a rubber sleeve to prevent the intrusion of the confining medium (oil). The specimens were fractured at 75 MPa confining pressure creating naturally fractured rough fault surface. To perform a series of subsequent stick-slip experiments, the faults were locked by increasing the confining pressure to 150 MPa. For the initial fracture and subsequent stick slip tests, the samples were loaded axially using a constant displacement rate of 0.02 mm/min = 0.33µm/s. Subsequent axial loading cycles were applied by advancing the piston at constant displacement rate resulting in an axial strain rate 3×10^{-6} s^{-1}. Displacement and axial force were recorded using a linear variable displacement transducer fixed to the piston and external/internal load cells, respectively.

We performed a series of tests on the three different Westerly granite samples WgN04, WgN05 and WgN07 containing rough faults (Goebel et al., 2012, 2013, 2014, 2015) but here we present data from an illustrative stick-slip test (WgN05) that was further studied in greater detail in Dresen et al. (2020) and Blanke et al. (2021). The recorded AE data, mechanical data and output parametric data from all three experiments are available in the associated data publication (Kwiatek and Goebel, 2023; see also Supplementary Information Figs. S5-S6 and Open Data section). The fault roughness in these experiments caused a complex stick-slip pattern with a variety of stress drops including five large slip events with large stress drops (LSD) of > 100 MPa preceded by a varying number of events with smaller slip and small stress drops (SSD), as determined from the axial stress data in Goebel et al. (2013 2015). They are shown in Figure 1 and Figs. S5-S6. Both LSDs and SSDs are accompanied by a large clipped signal on the AE data, representing relatively large laboratory events (see e.g. Fig. 3 in Goebel et al., 2012).

Loading and stick-slip events produced AEs, here indicating ~mm-scale fracturing and frictional processes occurring on the grain scale (cf. Blanke et al., 2021). AE activity was recorded by sixteen AE sensors with resonant frequency 2 MHz embedded in brass housings and glued directly to the specimen surface, securing an almost complete azimuthal coverage of AE events. The event waveforms were recorded in triggered mode at 10 MHz sampling rate with 16-bit amplitude resolution. Throughout the experiment, repetitive *P*-wave velocity measurements were performed using ultrasonic transmission providing a time-dependent velocity model composed of five equally-spaced horizontal layers (with associated velocity) and single measurement of averaged vertical velocity (Stanchits et al., 2006). The velocity model was updated every 30 s during the course of the experiment.

2.2 Mechanical behavior and AE response

We now describe the evolution of mechanical parameters and associated AE response for an illustrative sample WgN05 following the conventions presented already and discussed in Goebel et al. (2012, 2013, 2014, 2015). Mechanical evolution for samples WgN04 and WgN07 is presented in the supplementary information (Figs. S5-S6), and the input catalog data are available in the associated data publication (Kwiatek and Goebel, 2023). Sample WgN05 displayed large axial stress drops measured in the S1 direction of $\Delta\sigma > 100$ MPa, slip duration of $0.2 - 0.4$ s and slip velocity (corrected for machine stiffness) of at least $1.2 - 1.6$ mm/s, which is at least 1000 times larger than the applied loading rates (cf. section 2.1, Fig. 1, Supplementary Table S1). Note that peak slip velocities for LSDs were not resolved due to the limited sampling rate of the geomechanical data (10 Hz). All LSDs were followed by rapid initial reloading lasting ca. 50 s and a longer period of almost linear stress increase lasting typically no more than 1000 s. Further axial displacement beyond a yield point was accommodated by plastic deformation along the fault zone and in its surroundings (cf. Dresen et al., 2020). We attribute most of the deformation during this part of the loading to shear-enhanced compaction of the granular material forming the fault gouge (Kwiatek et al., 2014b; Goebel et al., 2017), as illuminated by the AE activity spreading over the whole fault surface (Fig. 1e, h).

Cm-scale roughness of the fault surface (cf. Fig. S7) results in multiple small slip events with low stress drops (SSDs), as defined in e.g. Goebel et al. (2012), which typically occur at elevated axial stress with S_1 > 400 MPa. The AE activity associated with these SSDs is distributed over significant parts or the entire fault surface (Fig. 1d, g). Stress drops of SSDs range $1<\Delta\sigma<20$ MPa and slip velocities range <0.05-0.2 mm/s (Supplementary Table S1). The lower observable limit of SSDs' stress

drops and slip velocity is due to the periodic noise of stress measurements caused by the servo-controlled MTS loading system.

The macroscopic displacement and stress drop recordings of LSDs and SSDs indicate detectable and relative movement of fault-bounding blocks across the entire fault surface (Supplementary Movie S1). The nucleation of both LSDs and SSDs is associated with extremely large AE events with clipped waveforms following the first P-wave arrival (e. g. Goebel et al., 2012, Fig. 3, Goebel et al., 2015, Fig. 5) and followed by a long coda wave indicating slip over the surface. This coda leads to a temporally higher AE event detection threshold due to low-frequency noise resulting from comminution and shearing of granular material and debris forming the fault surface while the fault is slipping (gray area in Fig. 1e). The duration of the AE system saturation time period lasts 20-120 ms and qualitatively scales with the duration of macroscopic slip and stress drop magnitude (cf. Supplementary Table S1). The enhanced low-frequency noise is expected to mask very early AE events directly following the LSDs.

In addition to LSD and SSD events resulting in externally measurable axial stress drops, we visually identified short-lasting bursts in AE activity due to slips confined in the sample that were mostly not recorded in the mechanical data (i.e. the externally measured axial stress drop is below $\Delta\sigma < 1$ MPa). These local confined slips with no externally measured stress drop (CSD) were attributed to local asperity failures providing a significant AE footprint with very localized AE activity that is most prominent in the early stick-slip cycles (cf. Fig. 1c, f; Supplementary Movie S1; see also Goebel et al., 2012, 2015). Like LSD and SSD, each CSD is also associated with a large AE event followed by smaller AEs (AE aftershocks) and occasionally preceded by increasing AE activity (AE foreshocks, see results section for details).

2.3 AE Catalog Development

The development of an AE catalog from the experimental data is an upgraded procedure originally developed by Stanchits et al., (2006). Here, we summarize key and new processing steps relevant for evaluating the time-dependent AE characteristics.

The first P-wave arrivals of AE events were picked automatically using the Akaike Information criterion followed by pick refinement using the modified Convolutional Neural Network picker (Ross et al., 2018) trained on past AE data sets. Based on a time-dependent quasi-anisotropic velocity model, the resolved picks were used to invert for hypocenter locations and origin time using a grid search algorithm paired with the Coyote optimization algorithm (Pierezan and Dos Santos Coelho, 2018). The hypocenter location accuracy is estimated to be about ±2 mm, constrained, in part, by

the selected Root-Mean-Square Deviation (RMSD) of travel time residuals (for the following analysis we selected locations with RMSD < 0.5 µs). Then, the first *P*-wave amplitudes were corrected for hypocentral distance and incidence angle and for the coupling quality of AE sensors using an ultrasonic calibration technique (Kwiatek et al., 2014a). The average AE amplitude and AE magnitude were calculated from first P-wave amplitudes (Zang et al., 1998):

$$\underline{A_{AE}} = \frac{1}{n}\left(\sum_{i=1}^{n}(A_i R_i)^2\right)^{0.5}, \quad (1)$$

$$M_{AE} = log_{10}(\underline{A_{AE}}), \quad (2)$$

where A_i and R_i are corrected first P-wave amplitude and source-receiver distance for sensor i, respectively (cf. Dresen et al., 2020). The here used AE magnitude estimate reveals relative size differences between AE events but it is not directly calibrated to the physical size of the events (cf. Goodfellow and Young, 2014; McLaskey et al., 2014; Yoshimitsu et al., 2014; Blanke et al., 2021).

For each AE event, a full moment tensor (FMT) inversion was performed using the hybridMT software and first P-wave amplitudes and durations of the first P-wave pulses (Kwiatek et al., 2016; Martínez-Garzón et al., 2017) corrected for coupling quality and incidence angle (Kwiatek et al., 2014a). The resulting FMTs were decomposed into isotropic and deviatoric parts (e.g. Vavryčuk, 2001; 2014). From the deviatoric part of the FMTs, we extracted the P-, T-, and B- axes directions (azimuths and plunges) and slip directions. A P- (T-, B-) axis plunge equal to 90° and 0° corresponds to the direction of maximum compression S_1 and the direction perpendicular to it, respectively. The two sets of nodal plane parameters (strike, dip, rake) were extracted from the deviatoric part of the seismic FMT of each AE event.

The analyzed catalog form WgN05 sample contains N=310,815 located AEs with N(M_{AE}>$M_{C,AE}$)=169,825 above the magnitude of completeness $M_{C,AE} = 1.5$ estimated using the goodness-of-fit method (Wiemer and Wyss, 2000) assuming that 95% of the catalog is explained by the Gutenberg-Richter power law. The FMTs were strongly quality-constrained, first at the input data selection (we only accepted input data where amplitude could be measured at all sensors), and then using as an uncertainty measure the maximum value of the diagonal elements of the covariance matrix normalized by the average AE amplitude, ε (see details hybridMT documentation, Kwiatek et al., (2016). Assuming, $\epsilon < 0.1$ and $N_{\text{stations}} = 14$, this resulted in a strongly reduced number of N(FMT)=17,963 high-quality FMTs. The resulting catalog containing origin time, AE location in the local Cartesian coordinate system of the sample, AE magnitude, FMT parameters including strike, dip, rake, the MT decomposition and orientation of P-, T- and B- axes, as well as

associated location and MT inversion uncertainties is available in an associated data publication (Kwiatek and Goebel, 2023).

2.4 Time series of AE parameters

For all three samples we analyzed the temporal evolution of a total of 10 parameters (features) derived from the AE catalog and defined onsets of informative changes of these parameters with regard to global damage and stress evolution and potential cross-correlations between different proxies. The selected parameters were utilized to characterize the development of local damage and stress evolution on and around the fault during the preparatory phases of five LSDs. The predictive AE-modeling of the time-to-failure, aggregating the input data from all three experiments, as well as unsupervised classification of the preparatory phase are subjects of separate manuscripts (Karimpouli et al., 2023a, b).

The temporal evolution of all AE parameters was calculated using sliding time windows of different lengths (ranging 1%-12% of the average length between consecutive LSDs, see Table 1) to better represent the development of short- and long-term processes. The calculated parameter values were assigned to the origin time of the last AE event included in each time window. We ignored time windows which overlap with the occurrence of LSDs to avoid mixing precursory AEs with those following LSD. In the following, we describe the 10 different AE parameters listed in Table 1 and subsequently used for tracking the preparatory processes.

(1) AE event rate: The AE event rate $\dot{N}$ (unit: [1/s]) has been calculated for the catalog of events with $M_{AE}>M_{AE,C}$ as the number of AEs divided by the duration of the moving time window. It represents the intensity of seismic activity across the whole fault surface and characterizes the damage (cf. Goebel et al., 2014).

(2) b-value: The slope from the magnitude-frequency Gutenberg-Richter (GR) relation indicates the proportion between the number of small and large AE events in a selected population. The *b*-value is calculated from AE events with magnitudes above the magnitude of completeness $M_{AE}>M_{AE,C}$ using the maximum likelihood method while including a correction for the histogram bin size (e.g. Lasocki and Papadimitriou, 2006). Changes in *b*-values are thought to be governed by rock damage evolution (e.g. Main, 1991), changes in local stress (Scholz, 1968; Schorlemmer et al., 2005), and geometric complexity and roughness (Goebel et al., 2013; 2017).

(3) d-value: The fractal dimension *d* from a population of AE hypocenters has been calculated using the boxcount algorithm (i.e. Minkowski–Bouligand dimension, see Moisy, 2022). We used

hypocentral locations [X, Y, Z] of AEs with location quality constrained by the RSMD<0.5 [µs]. The *d*-value characterizes the geometry of the AE spatial distribution of AE with *d*=3, *d*=2, and *d*=1 corresponding to volumetric, planar and linear Euclidean distribution of AE hypocenters, respectively. Contrary to the *d*-value estimated using correlation integral, which is sensitive to point-clustering of the hypocentral locations, the box-counting method solely responds to the bulk geometry of AE hypocenter distribution.

Clustering of AE events in space, time and magnitude domain: We identified clusters of AE events according to their space-time-magnitude nearest-neighbor proximity (Zaliapin et al., 2008; Zaliapin and Ben-Zion, 2013a; 2013b). Specifically, we investigated the proximity of an event *j* to an earlier event *i* in a combined space-time-magnitude domain (Baiesi and Paczuski, 2004) defined as:

$$\eta_{ij} = \{t_{ij}\left(r_{ij}\right)^{d} 10^{-bm_i}\}, t_{ij} > 0, \infty, t_{ij} \leq 0, \quad (3)$$

where $t_{ij} = t_j - t_i$ and r_{ij} are the temporal and spatial distances between the earthquakes i and j, respectively, b is the *b*-value from the GR distribution, d is the fractal dimension, both estimated as described above, and m_i is the magnitude of the earlier event in time. The scalar proximity η_{ij} between events can be expressed as the product of its temporal and spatial components scaled by the magnitude of the earlier event i:

$$\eta_{ij} = T_{ij} \cdot R_{ij}, \quad (4)$$

with $T_{ij} = t_{ij}10^{-qbm_i}$ and $R_{ij} = (r_{ij})^{d}10^{-(1-q)bm_i}, 0 \leq q \leq 1$. We fixed $q = 0.5$, providing equal magnitude weights to the scaled temporal and spatial distances. To estimate the spatial distance between events we used hypocentral locations. We denote η_j the shortest of the proximities between event j and all earlier events. The distributions of the nearest-neighbor proximities η_j in earthquake catalogs tend to be bimodal (Zaliapin and Ben-Zion, 2013a, Zaliapin and Ben-Zion, 2016; Martínez-Garzón et al., 2019). The mode with larger event proximities η_j corresponds to *background* Poissonian-like seismicity, while potentially appearing mode with smaller event proximities η_j indicates *clustered* events, i.e. foreshocks and aftershocks (Zaliapin et al., 2008). The separation threshold between these two modes is estimated by fitting a Gaussian mixture model (Supplementary Figure S2).

Using the above method, we identify AE clusters that are connected by proximity links smaller than the estimated threshold. Each AE connected to the parent by a link longer than the threshold is considered a *background* event and starts a new cluster. A *single* is a cluster that consists of one background event with no associated foreshocks or aftershocks, while multiple-event clusters are

called *families*. The largest event in each cluster is called *mainshock*; all events within the cluster before or after the mainshock are called *fore/after-shocks* (see Fig. 6 of Zaliapin and Ben-Zion, 2013a). Due to the short-term saturation of the AE recording system during large slip events LSD1-LSD5 (see more details in the results section), the clustering analyses have been performed separately for each phase P1-P5 (Fig. 1a). This means that early aftershocks from previous slip for phases P2-P5 are not well resolved, biasing the separation between foreshocks, aftershocks, mainshocks and singles shortly after the LSDs.

The temporal changes in AE clustering properties occurring on grain-scales have been analyzed using a sliding time window. We calculated temporal evolution of four parameters, including the **(4) median proximity** parameter η:

$$\hat{\eta} = median\{\eta_j\}, \quad (5)$$

defined as a median of the decimal logarithm scalar proximities (eq. 4) of AEs, and the fraction of AE **(5) foreshocks** (p_{FO}), **(6) aftershocks** (p_{AF}), and **(7) background (mainshocks and singles altogether)** (p_{MA}) in each examined time window (with $p_{AF}+p_{FO}+p_{MA}=1$).

The **(8) median fault plane variability** $\widehat{\psi_f}$ characterizes the level of heterogeneity in the distribution of the focal mechanisms (Martínez-Garzón et al., 2016; Goebel et al., 2017; Dresen et al., 2020). This is a generalization of rotation angle between pairs of focal mechanisms (Kagan, 2007) applied to an ensemble of pairs of AEs with focal mechanism solutions located nearby. A small 3D rotation angle (<20°) between the P/T/B axes of two mechanisms indicates a high degree of similarity, and 0° means they are identical.

We compute the spatial variability of focal mechanism similarity across the laboratory fault and rock sample. Spatial variability is determined from 20 nearest AE neighbors located within R<10 mm of the specific AE event by calculating the respective median 3D rotation angle between all focal mechanism pairs (e.g. for 20 AE focal mechanisms there are 190 pairs). This procedure was repeated for each AE event to resolve the spatial heterogeneity/similarity of focal mechanism variability across the whole fault plane. The focal mechanism variability for a particular time window was then estimated as the median of locally calculated values.

(9) Plunge of local maximum principal stress $\delta_{\sigma 1}$ and (10) local stress (orientation) variability $\widehat{\Psi_{\sigma ij}}$: Using calculated MTs we performed a linear stress tensor inversion using the STRESSINVERSE package (Vavryčuk, 2014). We follow the sign convention that compressive stress σ is positive with $\sigma_1 > \sigma_2 > \sigma_3$. Similarly to median fault plane variability $\widehat{\Psi_f}$, for each time window, we first

calculated the spatial distribution of local stress tensors for each location where at least 40 focal mechanisms were available within a 10 mm distance. The input focal mechanism data were resampled and then inverted 200 times by randomly selecting either of the two nodal planes for each focal mechanism, suppressing the problem of fault plane ambiguity (e.g. Martínez-Garzón et al., 2014) in the input focal mechanism data. From this we obtained the spatial distribution of local stress tensors for a particular time window.

In the following, for each local stress tensor, we extracted the plunge of maximum principal stress $\delta_{\sigma 1}$ which is given by the eigenvector corresponding to the largest eigenvalue of the input stress tensor. Finally, we averaged maximum principal stress plunges from the whole fault surface. For plunges of $\delta_{\sigma 1}$= 90° the local principal stresses averaged over the sample surface are aligned with the macroscopic vertical loading stress direction S_1.

The second parameter describing the local stress tensors is the tensor variability $\widehat{\Psi_{\sigma ij}}$, which was calculated with the same procedure as for the focal mechanism variability estimation. For each time window, we calculated the median out of an ensemble of rotation angles between all possible pairs of local stress tensors. Low values of $\widehat{\Psi_{\sigma ij}}$ suggest that local stress tensor orientations over the fault surface are similar.

3 Results

Here we present and describe representative time series for each of the above parameters describing the evolution of the fault system in sample WgN05. The results for samples WgN04 and WgN07 are presented in the supplementary information (Figs. S5-S6).

3.1 AE Rates

The AE rates display a short-term (within each phase P1-P5 leading to the LSD) as well as a long-term (across whole experiment) evolution with progressive deformation of the sample (Figure 2b). The long-term evolution is characterized by an overall decrease of peak AE rates $\dot{N}$ (Fig. 2b). The individual phases P1-P5 preceding LSD1-LSD5 display exponentially increasing $\dot{N}$ when approaching failure (Fig. 2b). The LSD nucleation point is illuminated by a large AE event located using P-wave arrivals. Once the elevated noise from saturation of the AE system drops to background level, AE aftershocks become visible, displaying a $1/T^p$ (Omori-type) decrease of AE rates typically lasting no more than about 20 seconds following the actual stress drop (cf. Supplementary Figure S1). The aftershock rates then decrease with consecutive LSDs suggesting bulk smoothing of the fault surface.

372 The increase of AE rates $\dot{N}$ during each phase P1-P5 is punctuated by multiple short-lasting bursts of
373 AE activity following SSDs and CSDs characterized by AE rates decreasing as $1/T^p$ over a short period
374 of time (typically < 10 s, Figure S1). All SSDs and all but one CSD show no acceleration of AE rates up
375 to failure (cf. Supplementary Figure S1). Only the second CSD (T=3672.8 s) that occurred in phase P1
376 show a visible acceleration of AE rates (Supplementary Figure S1b). The SSDs and CSDs tend to
377 reduce the overall long-term AE rates in phases preceding LSDs (Figure 1b). AE rates are closely
378 related to slip rate at any spatial scale (i.e. at long-scale representing the sample size and the short-
379 scale representative of asperity size). However, there is no clear relation of peak AE rates with stress
380 drop magnitude.

381 3.2 Gutenberg-Richter *b*-value

382 The temporal evolution of the *b*-value (Fig. 2c) displays low *b*-values associated with CSD and SSD
383 events (cf. Goebel et al., 2013) through all phases P1-P5, but especially during P1 and P2. This
384 suggests that the change in *b*-value acts as a proxy generally indicating small- (cm-scale) local
385 ruptures confined in the sample at high levels of stress. In general, a decrease in *b*-value indicates an
386 approach to system-wide failure (LSD).

387 From phase P3 onwards, CSDs and SSDs are less prominent and the temporal trends of the *b*-value
388 become somewhat more uniform and gradual. This may reflect a global conditioning process of the
389 whole fault surface, progressive localization and overall reduction of the fault roughness at the scale
390 of the whole sample. In P3-P5, prior to the LSDs, the *b*-values visibly decrease, and then recover to
391 *b*=1.4-1.6 during the initial part of the subsequent loading cycle. The amplitude of the *b*-value
392 recovery following the LSD is likely affected by the saturation of the AE acquisition system which
393 masks smaller aftershocks immediately following LSD, presumably reducing the jump in *b*-value in
394 early post-slip phases. The decreasing *b*-value before some of the CSDs and SSDs typically becomes
395 more evident if the AEs are additionally spatially constrained to those related to the activation of
396 specific patches (see e.g. Goebel et al., 2012). Overall, the localized slips (CSDs and SSDe) tend to be
397 preceded by a *b*-value decrease irrespective of the amplitude of macroscopic slip, thus the *b*-value is
398 predominantly sensitive to the long-term temporal evolution (sample-wide) as well as cm-scale
399 (asperity size) changes throughout the first phases P1-P2.

400 3.3 Fractal dimension

401 The *d*-values derived with the boxcounting method are primarily sensitive to the spatial distribution
402 of AEs, and less sensitive to AE density, as for example *d*-value estimations based on the correlation

integral. A *d*-value of about 2.0 corresponds to an AE hypocenter distribution across the fault surface. In contrast, *d*-values < 2.0 indicate formation of distinct AE lineaments or clusters within the fault zone. The evolution of the *d*-value during individual stick-slip cycles leads to a general increase of the *d*-value ahead of each major LSD, signifying the overall increase in the AE activity across the entire fault surface as a consequence of the increased contact area between the two faces of the fault. The AE activity immediately following the LSDs is characterized by higher *d*-values that quickly decrease within the first 50-100 seconds following the LSD. This may be due to fault dilation associated with large slip and a destruction of small-scale asperities in contact reducing AE activity to linear or isolated clusters indicating larger asperities. As loading and shear-enhanced compaction across the fault resumes, the *d*-value increases again.

Interestingly, over stick-slip phases P1-P5 the *d*-values decrease. Local peak *d*-values are typically reached just prior to LSDs and they decrease from about 2.0 to 1.7 with consecutive LSDs. Concurrently, we observe development of a diagonal step-over (cf. Fig. S7) that in the later phases hosts the majority of AE activity forming a quasi-linear distribution of activity and depletion in AE activity elsewhere. Our observation suggests that *d*-value is primarily sensitive to changes over the length of the whole sample, collecting information from the geometrical distribution of AE events across the whole fault surface.

3.4 Clustering properties

The spatial distribution of AE hypocenters allows identifying transient AE clusters forming at small-scale mm- to cm-scale asperities characterizing the rough topography of the fault surfaces (Figure S7, see also Goebel et al., 2012, 2015). All phases P1-P5 show generally similar trends in the evolution of the median event proximity $\hat{\eta}$ parameter (Figure 3b), which signifies the level of event clustering in the combined space, time and magnitude domain. During the initial part of each stick-slip cycle at low axial stress, the median event proximity $\hat{\eta}$ is relatively large. This indicates a dominance of diffuse background activity suggesting random distribution of events in time, space and magnitude domains over the surface. This agrees with the high proportion of mainshocks and *singles* in the AE catalog observed during the initial portion of each stick-slip cycle (Fig. 3c).

With progressive loading and when approaching LSD failure, the AE rates increase and the median event proximity $\hat{\eta}$ displays a transient decrease, indicating a progressive localization of AE activity (Fig. 3b). This observation is consistent with other laboratory studies (e.g. Bolton et al., 2023; Marty et al., 2023). Concurrently, we observe a decreasing proportion of mainshocks and singles that are superseded by aftershocks and occasionally by foreshocks (Fig. 3c). The progressive localization and

increasing size of AE clusters before LSD failures agree with observed patterns before several Mw > 7 earthquakes in Baja and southern California (Ben-Zion and Zaliapin, 2020). The proportion of foreshocks clearly does not increase ahead of the LSD, and are instead correlated with the SSD and CSD occurrence. Likewise, an increase in AEs classified as aftershocks with progressive loading ahead of the LSD appears to be linked to the more frequent occurrence of SSDs and CSDs at higher axial stresses, rather than directly with the run-up to LSD.

Some SSDs and CSDs are preceded by a visible short-term drop in the median event proximity $\hat{\eta}$ signifying increased clustering, and all CSDs and SSD display strong space-time localization within up to 20 seconds after the slip followed by a transient $\hat{\eta}$ recovery (Figure 3c, Supplementary Figure S3). The amplitudes of temporal $\hat{\eta}$ changes before the CSD or SSD do not seem to correlate with the macroscopic stress drop that follows (cf. Fig. S3 and Table SS1). Accordingly, the short-lasting clustering episodes framing SSDs and CSDs are sometimes preceded by an increased proportion of AE events that are classified as foreshocks, especially in later loading phases. The SSDs and CSDs are always followed by an increased proportion of AE events classified as aftershocks (Supplementary Figure S4). The proportions of foreshocks, mainshock and aftershocks do not substantially evolve across several stick-slip cycles, despite the fact that the number of visible SSDs and CSDs responsible for clustered seismicity seem to reduce with time (cf. Fig. 3a with Fig. 3c).

Time periods directly following LSDs display strong clustering with complete lack of AE foreshocks replaced with AEs classified as mainshocks/singles and aftershocks. The proportion of clustered to background events (e.g. Martínez-Garzón et al., 2018) seems lower on average in comparison to that in the time periods following SSD and CSD, which reflects problems with classification of events in these time periods due to the saturation of the AE system. Nevertheless, in the time period following a LSD, the initially localized AE activity progressively delocalizes within 50-100 s and the next cycle starts, initially dominated by background seismicity. In summary, the evolution of clustering properties is associated predominantly with the life cycle of cm-scale asperities (cf. Fig. S7).

3.5 Fault plane variability

The observed AEs result from fracturing and frictional processes occurring on the grain scale (<mm scale). Consequently, the observed temporal evolution of fault plane variability $\widehat{\psi_f}$ (Figure 4) reflects the complex grain-scale (mm) micromechanics. This is because the parameter compares faulting kinematics of individual AE events located close by. In general, high $\widehat{\psi_f}$ values are observed during the entire experiment, reflecting a broad orientation distribution of focal mechanisms that

comprise mostly normal (parallel to fault dip) to strike-slip faulting mechanisms across the whole fault surface. During loading, fault variability mostly increases or fluctuates around a high level but, in some cases, $\widehat{\psi_f}$ decreases before LSD. The latter agrees with earlier observations of Dresen et al. (2020) and Goebel et al. (2017) indicating an increasing alignment of microslip planes ahead of LSD. However, in rough faults the process is far less prominent than observed for saw-cut faults (e.g. Goebel et al., 2017) In addition, $\widehat{\psi_f}$ seems largely unaffected by the occurrence of CSD or SSD events and does not show fundamental long-term evolution across many stick-slip phases. This suggests that the grain-scale roughness is largely preserved during the experiment.

3.6 Maximum principal stress orientation and stress variability

Stress tensor inversion from AE-derived focal mechanisms allows inferring the local orientation of the deviatoric stress tensor and a relative measurement of its eigenvalues. Changes in principal stress orientation in response to loading, averaged over the whole fault plane, are recorded with the $\delta_{\sigma 1}(t)$ (plunge) parameter, whereas heterogeneity of the local stress tensors is reflected in $\Psi_{\sigma ij}(t)$ parameter.

During the initial phase P1 the plunge of the maximum principal stress orientation $\delta_{\sigma 1}(t)$ resolved locally stays close to vertical. Subsequently, $\delta_{\sigma 1}(t)$ progressively deviates from the vertical direction as loading increases. Ignoring some short-period outliers, local plunges of the maximum principal stress roughly vary between 90° and 40° with respect to the vertical sample axis during loading and unloading. Excluding the stick-slip cycle associated with LSD4, we find a progressive rotation of the maximum principal stress during loading while approaching remaining LSDs. This rotation is likely due to shear-enhanced compaction and build-up of shear stress during loading near the fault surface, causing a local rotation of the stress tensor. The increasing local shear stresses are released during slip events, leading to back rotation of the local stresses towards the initial stress state that is observed in early part of the phases P2-P4, following the LSD1 and LSD3, respectively. The rotation of the principal stress axes in each stick-slip cycle is associated with a slow reduction in spatial heterogeneity of the local stress, as indicated by the decreasing stress variability coefficient $\widehat{\Psi_{\sigma ij}}$.

4 Discussion

Various large earthquakes were observed to be preceded by precursory deformation and foreshock seismicity on varying scales in space and time, but the observed patterns are diverse and do not always occur (e.g. Kanamori, 1981; Wu et al., 2013; Kato and Ben-Zion, 2021; Sykes, 2021; Kwiatek et al., 2023). Recent studies of laboratory data showed that the use of AI techniques and features

derived from AEs can open up new avenues towards forecasting laboratory earthquakes on smooth faults. However, the range of observable physical processes involved in the run-up to dynamic rupture and how they interact remain not well-understood, regardless of the scale (Ben-Zion, 2008, and references therein). Likewise, there is a need for physical understanding of the extracted data features used by AI techniques and assessment of their effectiveness in describing the run-up to failure, especially for rough faults (see overview in Karimpouli et al., 2023a, Johnson et al., 2021; Bolton et al., 2019; Lubbers et al., 2018; Picozzi and Iaccarino, 2021).

In this paper, we employ data from laboratory experiments and use AE-derived seismo-mechanical and statistical parameters to characterize the evolution of local damage, roughness, and stress in the immediate vicinity of a rough fault surface. In particular, we investigate whether our parameters contain information on the preparation process leading to large stress drops (LSD). The sizes of AEs recorded in laboratory experiments analyzed in this study range from M_W -7 to M_W -9 (Dresen et al., 2020; Blanke et al., 2021), being at least 3 units lower than the estimated magnitude of the large stick-slips (Dresen et al., 2020). A meta-analysis by Mignan (2014) suggested that such AE activity may include key precursory information related to large laboratory earthquakes. Field observations of processes leading to large earthquakes have been categorized as pre-slip, cascade, or localization phenomena, but recent studies point towards a case-specific combination of processes (see Cattania and Segall, 2021, and reviews in McLaskey, 2019; Kato and Ben-Zion, 2021). The physically-motivated parameters used in this study are shown to (I) collectively capture the deviation from long-lasting stable deformation towards a preparatory process of large unstable failure, and (II) enable high-resolution monitoring of local damage, roughness, and stress at different temporal and length scales. This allows us to identify the time in which the fault enters a critical stage during which a system-size dynamic rupture may seemingly occur at any time.

The stick-slip experiments are performed on a naturally fractured rock sample (Goebel et al., 2014, 2015). The fault surface (e.g. Fig. S7 for WgN05) displays high initial roughness representing a strongly segmented and juvenile fault in nature. This is in contrast to a smooth saw-cut surfaces which may be more representative of a fault with large displacement (cf. Goebel et al., 2017). As in many past experiments (see e.g. Harbord et al., 2017), slip events on a rough fault show a rich mechanical behavior. The large (LSD) and small (SSD) macroscopic slips of the whole or significant portions of the surface display varying durations and amplitudes reflecting fast and slow slip velocities as well as large and small stress drops (cf. Supplementary Table S1). Smaller slips confined within the fault surface (CSD) are highlighted solely by AE activity, but not with external readings. In consequence, the seismo-mechanical behavior generally shows much stronger or fractal-like

fluctuations compared to saw-cut faults in triaxial stick-slip experiments (cf. Goebel et al., 2015, 2017), and double-direct shear experiments containing gouge (e.g. Scuderi et al., 2017; Bolton et al., 2021). This highlights the need for a careful extraction of meaningful features/parameters from AE data describing the processes leading to system-size failure to enrich information on preparatory processes.

4.1 Fault roughness, damage and stress evolution

The complex evolution of fault damage, roughness and stress across multiple stick-slip cycles with progressive shearing is related to *grain-scale* comminution, gouge production and destruction of *small-scale* asperities that ultimately lead to generation of the persisting *large-scale* topography (cf. Goebel et al., 2012, 2015, 2017; Kwiatek et al., 2014b). Development of roughness at these different spatial scales has always some AE response (cf. Goebel et al., 2014). The length scale of the roughness/damage evolution processes may be captured with AE source parameters via their collective seismo-mechanical and statistical proxies (cf. Dresen et al., 2020; Blanke et al., 2021). In this study, grain-scale roughness behavior is represented by the fault plane variability, which captures the difference between focal mechanisms of neighboring events. The *small-scale* roughness evolution of small cm-scale asperities is observed with collective properties of AE activity such as event rates, and predominantly with (spatio-)temporal features including clustering and local-stress field orientation and variability. Finally, the development of the *large-scale* (>cm) topography is captured by long-term trends in the temporal evolution of global properties including *d*-value, *b*-value and event rates $\dot{\eta}$.

The complex long-term (across many stick-slip cycles) evolution of fault roughness is primarily documented in the spatio-temporal AE distribution (*d*-value) and localized damage indicators (*b*-value, AE rate, cf. Fig. 2), as presented in past studies (Goebel et al., 2013, 2017; Kwiatek et al., 2014b; Dresen et al., 2020). A decrease in local stress variability (Fig. 4c), the new parameter calculated using AE stress tensor inversion, confirms progressive smoothing of the large-scale fault surface. These parameters signify that fault roughness evolves substantially up to LSD2 but less in P3-P5. This is likely because after multiple slip events, small-scale asperities are progressively destroyed but a *large-scale* fault topography remains, as revealed by the post-mortem inspection of deformed samples (Fig. S7). Consequently, the later P3-P5 AE activity is focused on these larger asperities at the expense of a more uniform distribution on the fault. This results in a general *d*-value decrease across many stick-slip cycles converging towards d=1.6 close to the peak stresses for the last cycles.

The AE rate and *d*-value evolution towards higher values in each phase preceding LSD imply spreading of AE events across the fault (Fig. 2d) imposed by enhanced contact area between the granular material forming the fault zone at elevated normal load (Dieterich and Kilgore, 1996) (cf. Supplementary Movie S1). This is associated with a general *b*-value decrease within the stick-slip cycle, interpreted as a signature of increased stress (Schorlemmer et al., 2005; Goebel et al., 2013) or damage accumulation (e.g. Main, 1991). Anti-correlations of *b*- and *d*-values, as observed in our study, have been reported in similar experiments (Main, 1991, 1992). However, the *d*-values and *b*-values are also frequently linearly related through $D = 2b$ (Aki, 1981; King, 1983) as found in some studies of natural earthquakes (Wyss et al., 2004) and other laboratory experiments (e.g. Goebel et al., 2017). It is therefore conceivable that interpretation of *b*- and *d*-value correlations and trends should be considered case-dependent (see also Legrand, 2002) and sensitive to the methodology used. The evolution of the used parameters within one cycle towards the LSD is superposed with high-frequency variations. These originate from activation of *short-scale* asperities at high levels of axial load, visible as CSD and SSD events and associated transient clusters of AEs (cf. Supplementary Movie S1-S4).

Post-mortem surface observations suggest that *small-scale* asperities causing clustered AE activity have been progressively erased (cf. Goebel et al., 2012, 2015) but *grain-scale* roughness remained unchanged. The former is supported by general decrease of the local stress variability (small-*scale*) over several slips (Fig. 4c), although we do not observe significant evolution of the fault plane variability that is governed by *grain-scale* fracturing. High values of fault plane variability observed during the whole experiment, especially if compared with saw-cut faults (cf. Dresen et al., 2020), reflect complex, inter-granular processes related to shear-enhanced compaction of the granular material forming the fault zone (Kwiatek et al., 2014b). This indicates persistence of *grain-scale* sub-mm roughness of the stress field. The micromechanical *grain-scale* roughness evolution leads effectively to smoothing of the short-scale asperities, and the short-scale stress field, as indicated by the decreasing local stress variability.

Beyond P2 we note that fewer and smaller SSDs occur prior to LSDs. Our observations suggest that with progressive slip and smoothing of small-*scale* fault heterogeneities, the stress field across the whole fault surface becomes more uniform, as the length scale of large heterogeneities becomes more prominent. Increased contact area, and smoothing of the *small-scale* asperities responsible for local stress concentrations result in *large-scale* homogenization of the stress field while approaching the LSD. This agrees with findings from numerical modeling (Ben-Zion et al., 2003) as discussed further in the next section.

To summarize, we find that *grain-scale* (<mm) and *large-scale* (>cm) roughness remain largely unchanged across many slip events in contrast to the *small-scale* (mm-to-cm) roughness involving asperities distributed initially across the surface that are progressively erased with repeating slips.

4.2 Multi-scale preparatory process and intermittent criticality

Within single stick-slip cycles, the evolving space-time-magnitude correlation η_j of AEs indicates formation of distinct clusters (Fig. 3b). Together with progressive *b*-value decrease and increased event rates, the combined parameter evolution implies accelerating deformation and localization ahead of the LSDs, in agreement with observations from lab tests and field data across different scales (Das and Scholz, 1981; see e.g. Lei and Ma, 2014; Ben-Zion and Zaliapin, 2020; McBeck et al., 2022). Moreover, the exponentially increasing AE rates indicates accelerated seismic release (ASR), which is a non-universal earthquake precursory behavior (e.g. Bufe et al., 1994; Ben-Zion and Lyakhovsky, 2002; Mignan, 2011). However, the discussed set of parameters does not unequivocally signify the proximity to system-size events (LSDs), as similar trends are observable at smaller spatio-temporal scales before individual SSDs or even CSDs.

At about 85-90% of the maximum axial stress (i.e. hundreds of seconds before LSD, corresponding to the yield stress of the fault), the examined parameters tend to mostly fluctuate around a saturation level with occurrence of SSDs and CSDs. Such saturation level is already observed in the first cycle P1 starting with the first CSD (ca. 1500 seconds before the LSD1) at about 85% peak stress and 75% of failure time t_f. In addition, we observe that the length of the saturation period prior to failure shortens with each stick-slip cycle, suggesting that the duration over which stress and seismic parameters fluctuate depends on the temporal evolution of fault roughness and associated stress heterogeneity. At the saturation level, *b*-values and $\hat{\eta}$ remain mostly low as both tend to drop significantly in the last part of the loading cycle. Likewise, the clustered AE activity including AE foreshock-mainshock-aftershock sequences increases, resulting in a reduced proportion of background events (Fig. 3c). Clustered AE activity clearly associated with SSDs and CSDs typically consists of aftershocks and few foreshocks framing the mainshock, suggesting active stress interaction between events as stress transfer occurs across mm- to cm- length scales of the stress field associated with asperities (see next section).

The external axial stress S_1 fluctuates around a critical state between ~85% and peak stress. This has been described previously as intermittent criticality and was observed in nature and numerical models in combination with accelerated seismic release and decreasing *b*-value (cf. Ben-Zion et al., 2003; Bowman and Sammis, 2004). In particular, Ben-Zion et al. (2003) showed in simulations of

stress and seismicity on a large heterogeneous fault that towards the end of a seismic cycle, a critical (fractal-like) disorder of the stress field heterogeneity is reached over a broad range of scales. This is found in a representative model for the brittle crust (model F, see Ben-Zion et al., 2003), which is characterized by realistic dynamic weakening. In agreement with our results, any stress perturbation at a high stress level may trigger a small or system wide seismic event. The ultimate size of the event is conditioned on whether the stress level is sufficiently high over a large portion of the fault surface and smooth over this length scale, allowing the event to propagate. Other models of nucleation of large events on rough faults were proposed using, e.g., models of progressive depinning of local asperities collectively reaching the critical nucleation length (Lebihain et al., 2021) and partitioning of seismic and aseismic slip and their collective influence on asperities failure and ultimate nucleation (e.g. Cattania and Segall, 2021).

Following Ben-Zion et al., (2003), large-scale correlation of elevated stresses enables the generation of large events over a smoothed portion of the stress field. However, the nucleation of such instability remains a statistical event, as it can be in principle triggered by a small *small-scale* or even a *grain-scale* stress perturbation at the right location. The statistical fluctuations before triggering of large lab earthquakes involve CSD and SSD events. These events lead to local stress relaxation across limited portions of the fault and stress transfer to the surrounding regions (Fig. 5). The concentrated stress transfer near previous failure events is evidenced by significant clustering of AE activity forming foreshocks and aftershock sequences at high axial stresses once CSDs and SSDs become more frequent. The redistribution of stress and the stress drops due to CSDs and SSDs may cause the fault to temporarily retreat from the critical stress level. As loading continues, stress recovers and long-range stress correlations are reestablished leading eventually to a system size (LSD) event.

4.3 Earthquake interaction on different length scales

At the beginning of a stick slip cycle, distributed background activity represents >90% of the total AE activity (Fig. 3c). As loading increases, activity rates increase, background activity and *b*-values decrease and there is a progressive spatio-temporal localization of AE events approaching LSDs (Fig. 3b). This is accompanied by increasing slip along the fault. The observed evolution of event proximity and mainshock aftershock distribution may signal AEs triggering close to larger slip events.

Compared to smooth saw-cut faults where shear strain is localized and off-fault damage is minor, increasing fault roughness results in significant off-fault damage and a relatively broad damage zone (Goebel et al., 2017). As a result, shear strain is less localized compared to smooth faults and fault slip starts at lower shear stress. Therefore, precursory slip displays a larger fraction of aseismic

deformation compared to smooth faults that unlock only at significantly higher stresses (e.g. Dresen et al., 2020). For rough faults, the increase in shear stress, compaction and contact area of the fault surfaces results in activation of a growing number of asperities leading to CSDs and LSDs. High local stress concentrations ahead of CSDs and SSDs, as well as local stress redistribution following these events, produces observable event clustering/triggering (see e.g. Schoenball et al., 2012; Davidsen et al., 2017, 2021; Martínez-Garzón et al., 2018). In agreement with Davidsen et al., (2017, 2021), the local stress concentrations produce AE event interactions. This highlights the importance of local stress intensities that control the evolution of the investigated parameters and the role of inter-event triggering (Meredith and Atkinson, 1983; Davidsen et al., 2017).

AE aftershocks following LSDs are controlled by residual elastic strain energy, and also depend on differences in fault roughness and slip stability (Goebel et al., 2023). However, aftershocks are relatively scarce in the examined data with respect to those framing SSDs and CSDs. This is partially because very early AE aftershocks following LSD or SSD are masked by the saturation of the AE system with continuous noise consisting of abundant overlapping AEs lasting up to 100 ms (see Supplementary Table S1). However, in large slip events the entire fault blocks are displaced and strength across the interface is reduced to sliding friction. Since the LSD rupture reaches the sample size, no stress redistribution beyond the rupture periphery is possible, which is in contrast to the confined or some small-scale (SSD) ruptures where the stress is redistributed internally. This is visibly reducing the aftershock productivity after LSDs, as the stress associated with large rupture is effectively unloaded in the triaxial machine. This difference in behavior of LSD and SSD/CSD in terms of stress transfer poses some challenges for the analysis of aftershocks following LSD/SSD and CSD. This observation needs to be considered while training models forecasting the time-to-failure of laboratory tests. However, Karimpouli et al. (2023) showed that training machine learning models forecasting time-to-failure using carefully framed data is possible, and the effects of boundary conditions can be minimized.

5 Potential applications to earthquake forecasting

Many studies attempted to characterize precursory deformation preceding large earthquakes using changes in seismicity rate, accelerated release of seismic moment and energy, changes of *b*-values, and other parameters calculated from geodetic and seismic data along with other measurements (e.g. Varnes, 1989; Bolton et al., 2021; Bowman et al., 1998; Gulia et al., 2016; Acosta et al., 2018; Bentz et al., 2019; Picozzi and Iaccarino, 2021; Shreedharan et al., 2021). However, very few if any datasets on the field scale have enough resolution to allow tracking evolution of the parameters discussed in our study during the preparatory phase for large events. This gap may be reduced using

693 modern AI techniques that allow enhancing seismic catalogs (e.g. Mousavi and Beroza, 2022;
694 Trugman and Ross, 2023). This will provide new information on processes preceding large
695 earthquakes via, e.g., additional informative foreshocks (Mignan, 2014). Meanwhile, at the
696 laboratory scale, parameters calculated from continuous waveform data or event catalogs have
697 been used already to successfully forecast the evolution of shear stress, friction, or time-to-failure
698 (see e.g. Lubbers et al., 2018; McBeck et al., 2020, Johnson et al., 2021, and references therein). It is
699 important to note that the seismo-mechanical behavior of smooth laboratory faults differs from that
700 observed for rough faults. The former tends to display a simpler and repetitive behavior, which is
701 attributed to the homogeneity of the fault gouge layer (e.g. Lubbers et al., 2018; Johnson et al.,
702 2021) or structural simplicity of the fault surface (e.g. Kwiatek et al., 2014; Goebel et al., 2017).
703 Smooth faults also display clearly identifiable transitions from quasi stable deformation towards
704 rapid acceleration resulting in seismic slip. This is associated with a non-linear accelerating seismic
705 response, and considerably simplifies the training of ML algorithms. Even for such repetitive stick-
706 slip experiments on saw-cuts, it was found that fault gouge layers evolve during the experiments
707 reducing the time-to-failure forecasting quality (see discussion in Johnson et al., 2021).

708 Comparisons of past laboratory tests on saw-cut faults and rough faults including results
709 from this study highlight the crucial impact of fault structural heterogeneity or fault roughness,
710 related stress field heterogeneity, stress transfer, and their temporal, spatial and length-scale
711 evolution on our capability of forecasting large failure events. Faults evolve with progressive loading
712 over geological timescales, displaying a qualitatively comparable evolution of many parameters (e.g.
713 localization, *b*-value) regardless of their structural and mechanical complexity (Tchalenko, 1970; Ben-
714 Zion and Sammis, 2003). However, it is feasible to observe very different precursory signatures,
715 depending on fault structure (roughness, complexity) and other conditions (Ellsworth and Bulut,
716 2018; Huang et al., 2020; Kato and Ben-Zion, 2021; Kwiatek et al., 2023). For rough faults, our study
717 suggests that a combination of physics-based parameters, reinforced with ML techniques, can
718 indicate when the system is entering a critical stage. However, identifying the final stage
719 immediately preceding system-size earthquakes may not be possible in the intermittent criticality
720 framework and ultimately conditioned by the finite spatio-temporal resolution of the monitoring
721 capabilities. Additional parameters yet to be developed may allow a closer identification of the final
722 triggering of large events. In any case, the ability to forecast large natural earthquakes will benefit
723 from dense instrumentation around hazardous faults that provide higher resolution data (e.g., Ben-
724 Zion et al., 2022).

Based on our experimental observations, Karimpouli et al. (2023a) found that the derived parameter pool characterizing different aspects of AE event organization in space and time, damage, stress and roughness evolution, enabled developing and constraining multi-parameter models of time-to-failure forecasting for complex rough laboratory faults. This may be done even with a considerably lower amount of input data compared to the saw-cut faults. In addition, Karimpouli et al. (2023a) emphasize the importance of the new features characterizing local stress evolution derived from seismic moment tensors and stress tensor inversion of AEs in time-to-failure forecasting. Interestingly, their analysis highlights that the parameters are collectively important for the accuracy of time-to-failure prediction, but need not necessarily be correlated individually with time to failure. In other words, the developed neural networks benefit from utilization of seemingly unimportant, yet novel details supplied by some parameters to improve the ultimate prediction. Using unsupervised K-means clustering of the seismo-mechanical and statistical parameters developed here, Karimpouli et al. (2023b) showed that it is possible to automatically identify a transition from stable deformation to an intermittent criticality state, with the most significant parameters being clustering properties using the decomposition of Zaliapin and Ben-Zion (2013a, b) as well as seismicity rates. They observed that the developed unsupervised scheme is able to recognize even finer transient processes related to the activation of smaller asperities, and depicted with scaled-down versions of CSDs composed of even shorter and spatially more confined clusters of AEs. These machine-learning enhanced findings are important in the context of the intermittent criticality model of Ben-Zion et al. (2003) shown here to provide a framework that can help to explain our results. As the final large slip may be triggered by a very small stress perturbation at the right location, this would suggest that improving the forecasting of large events requires zooming-in further into the clustering processes of CSDs and searching for potential deviation from their behavior ahead of the main rupture.

Conclusions

We studied the preparatory processes preceding laboratory earthquakes on rough faults using an ensemble of 10 seismo-mechanical and statistical features. These physics-based parameters describe damage and stress evolution in the fault zone, localization processes, local micromechanics and earthquake interactions, as well as local stress field evolution and stress field heterogeneity.

The selected features enable understanding a diversity of processes occurring at different spatial and temporal scales during the preparatory phase preceding system-size laboratory earthquakes, these features can help constraining the input for multi-parameter AI-aided models of earthquake forecasting.

The developed set of precursory parameters highlights localization processes preparing system-size earthquakes. However, the parameters are sensitive to length scales of fault surface roughness and associated roughness of the stress field, both rapidly evolving in the course of an experiment. The spatio-temporal evolution of fault surface and stress roughness poses limitations on our ability to monitor and forecast the run-up to large laboratory earthquakes.

We identify a transition from stable deformation to an intermittent criticality state allowing the occurrence of large events. This stage is characterized by abundant AE activity highlighting persistent heterogeneity of the stress field at the sub-mm grain-scale. Spatio-temporal AE activity bursts indicate small confined slips in the sample marking a progressive breakdown of asperities. These confined slips superimpose and interact, collectively preparing the fault surface for a system-size slip by progressive smoothing the short- (mm-to-cm) scale stress field. Ultimately, the development of large-scale correlation of elevated stresses enables the propagation of a large slip event over the smoothed portion of the fault, triggered even by a minor stress perturbation.

A system-size earthquake occurring at a state of intermittent criticality is a statistical event that cannot be predicted deterministically. However, using a combination of the parameters described in this study allows identifying the onset time when a fault enters a critical stage. This may be improved with AI classification techniques using cross-scale, physics-based parameters to detect the critical state of a fault system.

Acknowledgments

We would like to thank G.C. Beroza, J. Davidsen, T. Weigel, D. Cas, H. Grover and B. Orlecka-Sikora for useful discussions during preparation of the manuscript. We acknowledge B. Fryer and two Anonymous Reviewers for valuable comments. The study was supported by the GeoForschungsZentrum Potsdam. The work of YBZ on analysis and interpretation was supported by the U. S. Department of Energy (Award DE-SC0016520). P.M.G acknowledges funding from the Helmholtz Young Investigators Group VH-NG-1232 (SAIDAN) and ERC Starting Grant -101076119 (QUAKEHUNTER).

Open Research

Seismic catalogs, moment tensor catalogs, raw waveform data, geomechanical data and associated information related to stick-slip experiments analyzed in this study are available at GFZ Data Services via separate data publication (CC-BY 4.0 license): Kwiatek and Goebel (2023).

References

Acosta, M., Passelègue, F. X., Schubnel, A., Madariaga, R., & Violay, M. (2019). Can Precursory Moment Release Scale With Earthquake Magnitude? A View From the Laboratory. Geophysical Research Letters, 46(22), 12927–12937. https://doi.org/10.1029/2019GL084744

Aki, K. (1981). A Probabilistic Synthesis of Precursory Phenomena, in *Earthquake Prediction*, pp. 566–574. [online] Available from: https://doi.org/10.1029/ME004p0566 (Accessed 27 April 2023)

Baiesi, M., and M. Paczuski (2004). Scale-free networks of earthquakes and aftershocks, *Phys. Rev. E* **69**, no. 6, 066106, doi 10.1103/PhysRevE.69.066106.

Bakun, W. H. et al. (2005). Implications for prediction and hazard assessment from the 2004 Parkfield earthquake, *Nature* **437**, no. 7061, 969–974, doi 10.1038/nature04067.

Bentz, S., P. Martínez-Garzón, G. Kwiatek, G. Dresen, and M. Bohnhoff (2019). Analysis of Microseismicity Framing ML > 2.5 Earthquakes at The Geysers Geothermal Field, California, *J. Geophys. Res. Solid Earth* doi 10.1029/2019JB017716.

Ben-Zion, Y. (2008). Collective Behavior of Earthquakes and Faults: Continuum-Discrete Transitions, Evolutionary Changes and Corresponding Dynamic Regimes, Rev. Geophysics, 46, RG4006, doi:10.1029/2008RG000260.

Ben-Zion, Y., and V. Lyakhovsky (2002). Accelerated Seismic Release and Related Aspects of Seismicity Patterns on Earthquake Faults, *Pure Appl. Geophys.* **159**, no. 10, 2385–2412, doi 10.1007/s00024-002-8740-9.

Ben-Zion, Y., and J. R. Rice (1997). Dynamic simulations of slip on a smooth fault in an elastic solid, *J Geophys Res* **102**, no. B8, 17771–17784.

Ben-Zion, Y., and C. G. Sammis (2003). Characterization of Fault Zones, *Pure Appl. Geophys.* **160**, no. 3–4, 677–715, doi 10.1007/PL00012554.

Ben-Zion, Y., and I. Zaliapin (2020). Localization and coalescence of seismicity before large earthquakes, *Geophys. J. Int.* **223**, no. 1, 561–583, doi 10.1093/gji/ggaa315.

Ben-Zion, Y., M. Eneva, and Y. Liu (2003). Large earthquake cycles and intermittent criticality on heterogeneous faults due to evolving stress and seismicity, *J. Geophys. Res. Solid Earth* **108**, no. B6, doi 10.1029/2002JB002121.

816 Ben-Zion, Y., G. Beroza, M. Bohnhoff, A.-A. Gabriel and P. M. Mai, 2022. A grand challenge
817 international infrastructure for earthquake science, Seis. Res. Lett., 93, 2967–2968, doi:
818 10.1785/0220220266.

819 Blanke, A., G. Kwiatek, T. H. W. Goebel, M. Bohnhoff, and G. Dresen (2021). Stress drop–magnitude
820 dependence of acoustic emissions during laboratory stick-slip, *Geophys. J. Int.* **224**, no. 2, 1371–
821 1380, doi 10.1093/gji/ggaa524.

822 Bolton, D. C., S. Shreedharan, J. Rivière, and C. Marone (2021). Frequency-Magnitude Statistics of
823 Laboratory Foreshocks Vary With Shear Velocity, Fault Slip Rate, and Shear Stress, *J. Geophys. Res.*
824 *Solid Earth* **126**, no. 11, e2021JB022175, doi 10.1029/2021JB022175.

825 Bolton, D. C., C. Marone, D. Saffer, and D. T. Trugman (2023). Foreshock properties illuminate
826 nucleation processes of slow and fast laboratory earthquakes. Nature Communications 14, 3859, doi
827 10.1038/s41467-023-39399-0

828 Bouchon, M., V. Durand, D. Marsan, H. Karabulut, and J. Schmittbuhl (2013). The long precursory
829 phase of most large interplate earthquakes, *Nat. Geosci.* **6**, no. 4, 299–302, doi 10.1038/ngeo1770.

830 Bowman, D. D., and C. G. Sammis (2004). Intermittent Criticality and the Gutenberg-Richter
831 Distribution, *Pure Appl. Geophys.* **161**, no. 9, 1945–1956, doi 10.1007/s00024-004-2541-z.

832 Bowman, D. D., G. Ouillon, C. G. Sammis, A. Sornette, and D. Sornette (1998). An observational test
833 of the critical earthquake concept, *J. Geophys. Res. Solid Earth* **103**, no. B10, 24359–24372, doi
834 10.1029/98JB00792.

835 Bufe, C. G., S. P. Nishenko, and D. J. Varnes (1994). Seismicity trends and potential for large
836 earthquakes in the Alaska-Aleutian region, *Pure Appl. Geophys.* **142**, no. 1, 83–99, doi
837 10.1007/BF00875969.

838 Cattania, C. and P. Segall (2021). Precursory Slow Slip and Foreshocks on Rough Faults. Journal of
839 Geophysical Research: Solid Earth 126, e2020JB020430, doi 10.1029/2020JB020430.

840 Corbi, F., L. Sandri, J. Bedford, F. Funiciello, S. Brizzi, M. Rosenau, and S. Lallemand (2019). Machine
841 Learning Can Predict the Timing and Size of Analog Earthquakes, *Geophys. Res. Lett.* **46**, no. 3, 1303–
842 1311, doi 10.1029/2018GL081251.

843 Das, S., and C. H. Scholz (1981). Theory of time-dependent rupture in the Earth, *J. Geophys. Res. Solid*
844 *Earth* **86**, no. B7, 6039–6051, doi 10.1029/JB086iB07p06039.

Davidsen, J., G. Kwiatek, E.-M. Charalampidou, T. H. W. Goebel, S. Stanchits, M. Rueck, and G. Dresen (2017). Triggering processes in rock fracture, *Phys. Rev. Lett.* **119**, 068501, doi 10.1103/PhysRevLett.119.068501.

Davidsen, J., T. Goebel, G. Kwiatek, S. Stanchits, J. Baró, and G. Dresen (2021). What Controls the Presence and Characteristics of Aftershocks in Rock Fracture in the Lab?, *J. Geophys. Res. Solid Earth* **126**, no. 10, e2021JB022539, doi 10.1029/2021JB022539.

Dieterich, J. H. (1978). Preseismic fault slip and earthquake prediction. Journal of Geophysical Research: Solid Earth 83, 3940–3948, doi 10.1029/JB083iB08p03940.

Dieterich, J. H., and B. Kilgore (1996). Implications of fault constitutive properties for earthquake prediction., *Proc. Natl. Acad. Sci.* **93**, no. 9, 3787–3794.

Dresen, G., G. Kwiatek, T. Goebel, and Y. Ben-Zion (2020). Seismic and Aseismic Preparatory Processes Before Large Stick–Slip Failure, *Pure Appl. Geophys.* doi 10.1007/s00024-020-02605-x.

Durand, V., S. Bentz, G. Kwiatek, G. Dresen, C. Wollin, O. Heidbach, P. Martínez-Garzòn, F. Cotton, M. Nurlu, and M. Bohnhoff (2020). A Two-Scale Preparation Phase Preceded an Mw 5.8 Earthquake in the Sea of Marmara Offshore Istanbul, Turkey, *Seismol. Res. Lett.* **91**, no. 6, 3139–3147, doi 10.1785/0220200110.

Ellsworth, W. L., and G. C. Beroza (1995). Seismic Evidence for an Earthquake Nucleation Phase, *Science* **268**, no. 5212, 851–855, doi 10.1126/science.268.5212.851.

Ellsworth, W. L., and F. Bulut (2018). Nucleation of the 1999 Izmit earthquake by a triggered cascade of foreshocks, *Nat. Geosci.* **11**, no. 7, 531–535, doi 10.1038/s41561-018-0145-1.

Geller, R. J., D. D. Jackson, Y. Y. Kagan, and F. Mulargia (1997). Earthquakes Cannot Be Predicted, *Science* **275**, no. 5306, 1616–1616, doi 10.1126/science.275.5306.1616.

de Geus, T. W. J., M. Popović, W. Ji, A. Rosso, and M. Wyart (2019). How collective asperity detachments nucleate slip at frictional interfaces, *Proc. Natl. Acad. Sci.* **116**, no. 48, 23977–23983, doi 10.1073/pnas.1906551116.

Goebel, T. H. W., T. W. Becker, D. Schorlemmer, S. Stanchits, C. Sammis, E. Rybacki, and G. Dresen (2012). Identifying fault heterogeneity through mapping spatial anomalies in acoustic emission statistics, *J. Geophys. Res. Solid Earth* **117**, no. B3, doi 10.1029/2011JB008763.

873 Goebel, T. H. W., D. Schorlemmer, T. W. Becker, G. Dresen, and C. G. Sammis (2013). Acoustic
874 emissions document stress changes over many seismic cycles in stick-slip experiments, *Geophys. Res.*
875 *Lett.* **40**, no. 10, 2049–2054, doi 10.1002/grl.50507.

876 Goebel, T. H. W., C. G. Sammis, G. Dresen, and D. Schorlemmer (2014). Off-fault damage and
877 acoustic emission distributions during the evolution of structurally-complex faults over series of
878 stick-slip events. Geophys. J. Int. 197, 1705–1718, doi 10.1093/gji/ggu074

879 Goebel, T. H. W., C. G. Sammis, T. W. Becker, G. Dresen, and D. Schorlemmer (2015). A Comparison
880 of Seismicity Characteristics and Fault Structure Between Stick–Slip Experiments and Nature. Pure
881 and Applied Geophysics 172, 2247–2264, doi 10.1007/s00024-013-0713-7
882
883 Goebel, T. H. W., G. Kwiatek, T. W. Becker, E. E. Brodsky, and G. Dresen (2017). What allows seismic
884 events to grow big?: Insights from b-value and fault roughness analysis in laboratory stick-slip
885 experiments, *Geology* **45**, no. 9, 815–818, doi 10.1130/G39147.1.

886 Goebel, T. H. W., E. E. Brodsky, and G. Dresen (2023). Fault Roughness Promotes Earthquake-Like
887 Aftershock Clustering in the Lab, *Geophys. Res. Lett.* **50**, no. 8, e2022GL101241, doi
888 10.1029/2022GL101241.

889 Goodfellow, S. D., and R. P. Young (2014). A laboratory acoustic emission experiment under in situ
890 conditions, *Geophys. Res. Lett.* **41**, no. 10, 3422–3430, doi 10.1002/2014GL059965.

891 Gounon, A., S. Latour, J. Letort, and S. El Arem (2022). Rupture Nucleation on a Periodically
892 Heterogeneous Interface, *Geophys. Res. Lett.* **49**, no. 20, e2021GL096816, doi
893 10.1029/2021GL096816.

894 Guérin-Marthe, S., S. Nielsen, R. Bird, S. Giani, and G. Di Toro (2019). Earthquake Nucleation Size:
895 Evidence of Loading Rate Dependence in Laboratory Faults, *J. Geophys. Res. Solid Earth* **124**, no. 1,
896 689–708, doi 10.1029/2018JB016803.

897 Gulia, L., T. Tormann, S. Wiemer, M. Herrmann, and S. Seif (2016). Short-term probabilistic
898 earthquake risk assessment considering time-dependent b values, *Geophys. Res. Lett.* **43**, no. 3,
899 1100–1108, doi 10.1002/2015GL066686.

900 Harbord, C. W. A., S. B. Nielsen, N. De Paola, and R. E. Holdsworth (2017). Earthquake nucleation on
901 rough faults, *Geology* **45**, no. 10, 931–934, doi 10.1130/G39181.1.

Hirose, F., K. Tamaribuchi, and K. Maeda (2021). Characteristics of Foreshocks Revealed by an Earthquake Forecasting Method Based on Precursory Swarm Activity, *J. Geophys. Res. Solid Earth* **126**, no. 9, e2021JB021673, doi 10.1029/2021JB021673.

Huang, H., L. Meng, R. Bürgmann, W. Wang, and K. Wang (2020). Spatio-temporal foreshock evolution of the 2019 M 6.4 and M 7.1 Ridgecrest, California earthquakes, *Earth Planet. Sci. Lett.* **551**, 116582, doi 10.1016/j.epsl.2020.116582.

Hulbert, C., B. Rouet-Leduc, P. A. Johnson, C. X. Ren, J. Rivière, D. C. Bolton, and C. Marone (2019). Similarity of fast and slow earthquakes illuminated by machine learning, *Nat. Geosci.* **12**, no. 1, 69–74, doi 10.1038/s41561-018-0272-8.

Johnson, P. A. et al. (2021). Laboratory earthquake forecasting: A machine learning competition, *Proc. Natl. Acad. Sci.* **118**, no. 5, e2011362118, doi 10.1073/pnas.2011362118.

Kagan, Y. Y. (2007). Simplified algorithms for calculating double-couple rotation, *Geophys. J. Int.* **171**, no. 1, 411–418.

Kanamori, H. (1981). The Nature of Seismicity Patterns Before Large Earthquakes, in *Earthquake Prediction*, pp. 1–19.

Karimpouli, S., D. Caus, H. Grover, P. Martínez-Garzón, M. Bohnhoff, G. C. Beroza, G. Dresen, T. Goebel, T. Weigel, and G. Kwiatek (2023a). Explainable machine learning for labquake prediction using catalog-driven features. Earth and Planetary Science Letters 622, 118383, doi 10.1016/j.epsl.2023.118383.

Karimpouli, S., D., G. Kwiatek, P. Martínez-Garzón, G. Dresen, and M. Bohnhoff (2023b). Unsupervised clustering of catalog-driven features for characterizing temporal evolution of labquake stress. Geophysical Journal International (submitted).

Kato, A., and Y. Ben-Zion (2021). The generation of large earthquakes, *Nat. Rev. Earth Environ.* **2**, no. 1, 26–39, doi 10.1038/s43017-020-00108-w.

Kato, A., K. Obara, T. Igarashi, H. Tsuruoka, S. Nakagawa, and N. Hirata (2012). Propagation of Slow Slip Leading Up to the 2011 Mw 9.0 Tohoku-Oki Earthquake, *Science* **335**, no. 6069, 705–708, doi 10.1126/science.1215141.

King, G. (1983). The accommodation of large strains in the upper lithosphere of the earth and other solids by self-similar fault systems: the geometrical origin of b-Value, *Pure Appl. Geophys.* **121**, no. 5, 761–815, doi 10.1007/BF02590182.

Kwiatek, G., E.-M. Charalampidou, and G. Dresen (2014a). An improved method for seismic moment tensor inversion of acoustic emissions through assessment of sensor coupling and sensitivity to incidence angle, *Int. J. Rock Mech. Min. Sci.* **65**, 153–161, doi 10.1016/j.ijrmms.2013.11.005.

Kwiatek, G., T. H. W. Goebel, and G. Dresen (2014b). Seismic moment tensor and b value variations over successive seismic cycles in laboratory stick-slip experiments, *Geophys. Res. Lett.* **41**, 5838–5846, doi 10.1002/2014GL060159.

Kwiatek, G., P. Martínez-Garzón, and M. Bohnhoff (2016). HybridMT: A MATLAB/Shell Environment Package for Seismic Moment Tensor Inversion and Refinement, *Seismol. Res. Lett.* **87**, no. 4, 964–976, doi 10.1785/0220150251.

Kwiatek, G., P. Martínez-Garzón, D. Becker, G. Dresen, F. Cotton, G. C. Beroza, D. Acarel, S. Ergintav, and M. Bohnhoff (2023). Months-long seismicity transients preceding the 2023 MW 7.8 Kahramanmaraş earthquake, Türkiye. Nat. Commun. 14, 7534, doi 10.1038/s41467-023-42419-8

Kwiatek, G. and T. Goebel (2023): Acoustic Emission and Seismic moment tensor catalogs associated with triaxial stick-slip experiments performed on the Westerly Granite samples [Dataset]. GFZ Data Services. doi 10.5880/GFZ.4.2.2023.003, Temporary link (will be edited during final proof check): https://dataservices.gfz-potsdam.de/panmetaworks/review/cf90017dac80dc3ebc19ae2b444c0e750112487de501a98c736154da55493ada/

Kwiatek, G., P. Martínez-Garzón, D. Becker, G. Dresen, F. Cotton, G.C. Beroza, D. Acarel, S. Ergintav and M. Bohnhoff (2023). Months-long seismicity transients preceding the 2023 Mw7.8 Kahramanmaraş earthquake, Türkiye. Nature Communications, doi 10.1038/s41467-023-42419-8.

Lasocki, S., and E. E. Papadimitriou (2006). Magnitude distribution complexity revealed in seismicity from Greece, *J. Geophys. Res. Solid Earth* **111**, no. B11, doi 10.1029/2005JB003794.

Latour, S., C. Voisin, F. Renard, E. Larose, S. Catheline, and M. Campillo (2013). Effect of fault heterogeneity on rupture dynamics: An experimental approach using ultrafast ultrasonic imaging, *J. Geophys. Res. Solid Earth* **118**, no. 11, 5888–5902, doi 10.1002/2013JB010231.

958 Lebihain, M., T. Roch, M. Violay, and J.-F. Molinari (2021). Earthquake Nucleation Along Faults With
959 Heterogeneous Weakening Rate. Geophysical Research Letters 48, e2021GL094901, doi
960 10.1029/2021GL094901

961 Leeman, J. R., C. Marone, and D. M. Saffer (2018). Frictional Mechanics of Slow Earthquakes, *J.*
962 *Geophys. Res. Solid Earth* **123**, no. 9, 7931–7949, doi 10.1029/2018JB015768.

963 Legrand, D. (2002). Fractal Dimensions of Small, Intermediate, and Large Earthquakes, *Bull. Seismol.*
964 *Soc. Am.* **92**, no. 8, 3318–3320, doi 10.1785/0120020025.

965 Lei, X., and S. Ma (2014). Laboratory acoustic emission study for earthquake generation process,
966 *Earthq. Sci.* **27**, no. 6, 627–646, doi 10.1007/s11589-014-0103-y.

967 Lippiello, E., C. Godano, and L. de Arcangelis (2019). The Relevance of Foreshocks in Earthquake
968 Triggering: A Statistical Study, *Entropy* **21**, no. 2, doi 10.3390/e21020173.

969 Lockner, D. (1993). The role of acoustic emission in the study of rock fracture, *Int. J. Rock Mech. Min.*
970 *Sci. Geomech. Abstr.* **30**, no. 7, 883–899, doi 10.1016/0148-9062(93)90041-B.

971 Lubbers, N., D. C. Bolton, J. Mohd-Yusof, C. Marone, K. Barros, and P. A. Johnson (2018). Earthquake
972 Catalog-Based Machine Learning Identification of Laboratory Fault States and the Effects of
973 Magnitude of Completeness, *Geophys. Res. Lett.* **45**, no. 24, 13,269-13,276, doi
974 10.1029/2018GL079712.

975 Main, I. G. (1991). A modified Griffith criterion for the evolution of damage with a fractal distribution
976 of crack lengths: application to seismic event rates and b-values, *Geophys. J. Int.* **107**, no. 2, 353–362,
977 doi 10.1111/j.1365-246X.1991.tb00830.x.

978 Main, I. G. (1992). Damage mechanics with long-range interactions: correlation between the seismic
979 b-value and the fractal two-point correlation dimension, *Geophys. J. Int.* **111**, no. 3, 531–541, doi
980 10.1111/j.1365-246X.1992.tb02110.x.

981 Martínez-Garzón, P., G. Kwiatek, M. Ickrath, and M. Bohnhoff (2014). MSATSI: A MATLAB Package
982 for Stress Inversion Combining Solid Classic Methodology, a New Simplified User- Handling, and a
983 Visualization Tool, *Seismol. Res. Lett.* **85**, no. 4, 896–904, doi 10.1785/0220130189.

984 Martínez-Garzón, P., Y. Ben-Zion, N. Abolfathian, G. Kwiatek, and M. Bohnhoff (2016). A refined
985 methodology for stress inversions of earthquake focal mechanisms, *J. Geophys. Res. Solid Earth* **121**,
986 no. 12, 8666–8687, doi 10.1002/2016JB013493.

Martínez-Garzón, P., G. Kwiatek, M. Bohnhoff, and G. Dresen (2017). Volumetric components in the earthquake source related to fluid injection and stress state, *Geophys. Res. Lett.* **44**, no. 2, 800–809, doi 10.1002/2016GL071963.

Martínez-Garzón, P., I. Zaliapin, Y. Ben-Zion, G. Kwiatek, and M. Bohnhoff (2018). Comparative Study of Earthquake Clustering in Relation to Hydraulic Activities at Geothermal Fields in California, *J. Geophys. Res. Solid Earth* **123**, no. 5, 4041–4062, doi 10.1029/2017JB014972.

Martínez-Garzón, P., Y. Ben-Zion, I. Zaliapin and M. Bohnhoff, 2019. Seismic clustering in the Sea of Marmara: Implications for monitoring earthquake processes, Tectonophysics, 768, UNSP 228176, doi: 10.1016/j.tecto.2019.228176.

Marty, S., A. Schubnel, H. S. Bhat, J. Aubry, E. Fukuyama, S. Latour, S. Nielsen, and R. Madariaga (2023). Nucleation of Laboratory Earthquakes: Quantitative Analysis and Scalings. Journal of Geophysical Research: Solid Earth 128, e2022JB026294, doi 10.1029/2022JB026294

McBeck, J., J. M. Aiken, Y. Ben-Zion and F. Renard, 2020. Predicting the proximity to macroscopic failure in dynamic X-ray tomography triaxial compression experiments on rocks, Earth Planet. Sci. Lett., 543, Article 116344, doi: 10.1016/j.epsl.2020.116344.

McBeck, J., Y. Ben-Zion, and F. Renard (2021). Fracture Network Localization Preceding Catastrophic Failure in Triaxial Compression Experiments on Rocks, *Front. Earth Sci.* **9**, doi 10.3389/feart.2021.778811.

McBeck, J., Y. Ben-Zion, and F. Renard (2022). Volumetric and shear strain localization throughout triaxial compression experiments on rocks, *Tectonophysics* **822**, 229181, doi 10.1016/j.tecto.2021.229181.

McLaskey, G. C. (2019). Earthquake Initiation From Laboratory Observations and Implications for Foreshocks, *J. Geophys. Res. Solid Earth* **124**, no. 12, 12882–12904, doi 10.1029/2019JB018363.

Mclaskey, G. C., and F. Yamashita (2017). Slow and fast ruptures on a laboratory fault controlled by loading characteristics, *J. Geophys. Res. Solid Earth* **122**, no. 5, 3719–3738, doi 10.1002/2016JB013681.

McLaskey, G. C., B. D. Kilgore, D. A. Lockner, and N. M. Beeler (2014). Laboratory Generated M -6 Earthquakes, *Pure Appl. Geophys.* **171**, no. 10, 2601–2615, doi 10.1007/s00024-013-0772-9.

1015 Meng, H., and W. Fan (2021). Immediate Foreshocks Indicating Cascading Rupture Developments for
1016 527 M 0.9 to 5.4 Ridgecrest Earthquakes, *Geophys. Res. Lett.* **48**, no. 19, e2021GL095704, doi
1017 10.1029/2021GL095704.

1018 Meredith, P. G., and B. K. Atkinson (1983). Stress corrosion and acoustic emission during tensile
1019 crack propagation in Whin Sill dolerite and other basic rocks, *Geophys. J. Int.* **75**, no. 1, 1–21, doi
1020 10.1111/j.1365-246X.1983.tb01911.x.

1021 Mignan, A. (2011). Retrospective on the Accelerating Seismic Release (ASR) hypothesis: Controversy
1022 and new horizons, *Tectonophysics* **505**, no. 1, 1–16, doi 10.1016/j.tecto.2011.03.010.

1023 Mignan, A. (2012). Seismicity precursors to large earthquakes unified in a stress accumulation
1024 framework, *Geophys. Res. Lett.* **39**, no. 21, doi 10.1029/2012GL053946.

1025 Mignan, A. (2014). The debate on the prognostic value of earthquake foreshocks: A meta-analysis,
1026 *Sci. Rep.* **4**, no. 1, doi 10.1038/srep04099.

1027 Mizrahi, L., S. Nandan, W. Savran, S. Wiemer, and Y. Ben-Zion (2023). Question-Driven Ensembles of
1028 Flexible ETAS Models, *Seismol. Res. Lett.* **94**, no. 2A, 829–843, doi 10.1785/0220220230.

1029 Moisy, F. (2022). boxcount, https://www.mathworks.com/matlabcentral/fileexchange/13063-
1030 boxcount

1031 Morad, D., A. Sagy, Y. Tal, and Y. H. Hatzor (2022). Fault roughness controls sliding instability, *Earth*
1032 *Planet. Sci. Lett.* **579**, 117365, doi 10.1016/j.epsl.2022.117365.

1033 Mousavi, S. M., and G. C. Beroza (2022). Deep-learning seismology, *Science* **377**, no. 6607,
1034 eabm4470, doi 10.1126/science.abm4470.

1035 Ogata, Y. (1999). Seismicity Analysis through Point-process Modeling: A Review, *Pure Appl. Geophys.*
1036 **155**, no. 2, 471–507, doi 10.1007/s000240050275.

1037 Ogata, Y., and K. Katsura (2012). Prospective foreshock forecast experiment during the last 17 years,
1038 *Geophys. J. Int.* **191**, no. 3, 1237–1244, doi 10.1111/j.1365-246X.2012.05645.x.

1039 Ohnaka, M. (1992). Earthquake source nucleation: A physical model for short-term precursors,
1040 *Tectonophysics* **211**, no. 1, 149–178, doi 10.1016/0040-1951(92)90057-D.

Ohnaka, M., and L. Shen (1999). Scaling of the shear rupture process from nucleation to dynamic propagation: Implications of geometric irregularity of the rupturing surfaces, *J. Geophys. Res. Solid Earth* **104**, no. B1, 817–844, doi 10.1029/1998JB900007.

Okubo, P. G. and J. H. Dieterich (1984). Effects of physical fault properties on frictional instabilities produced on simulated faults. Journal of Geophysical Research: Solid Earth 89, 5817–5827, doi 10.1029/JB089iB07p05817.

Picozzi, M., and A. G. Iaccarino (2021). Forecasting the Preparatory Phase of Induced Earthquakes by Recurrent Neural Network, *Forecasting* **3**, no. 1, 17–36, doi 10.3390/forecast3010002.

Pierezan, J., and L. Dos Santos Coelho (2018). Coyote Optimization Algorithm: A New Metaheuristic for Global Optimization Problems, in *2018 IEEE Congress on Evolutionary Computation (CEC)*, pp. 1–8.

Ross, Z. E., M.-A. Meier, and E. Hauksson (2018). P Wave Arrival Picking and First-Motion Polarity Determination With Deep Learning, *J. Geophys. Res. Solid Earth* **123**, no. 6, 5120–5129, doi 10.1029/2017JB015251.

Rouet-Leduc, B., C. Hulbert, N. Lubbers, K. Barros, C. J. Humphreys, and P. A. Johnson (2017). Machine Learning Predicts Laboratory Earthquakes, *Geophys. Res. Lett.* **44**, no. 18, 9276–9282, doi 10.1002/2017GL074677.

Schoenball, M., C. Baujard, T. Kohl, and L. Dorbath (2012). The role of triggering by static stress transfer during geothermal reservoir stimulation, *J. Geophys. Res. Solid Earth* **117**, no. B9, doi 10.1029/2012JB009304.

Scholz, C. H. (1968). The frequency-magnitude relation of microfracturing in rock and its relation to earthquakes, *Bull Seism. Soc Am* **58**, no. 1, 399–415.

Schorlemmer, D., S. Wiemer, and M. Wyss (2005). Variations in earthquake-size distribution across different stress regimes, *Nature* **437**, no. 7058, 539–542, doi 10.1038/nature04094.

Schurr, B. et al. (2014). Gradual unlocking of plate boundary-controlled initiation of the 2014 Iquique earthquake, *Nature* **512**, no. 7514, 299–302, doi 10.1038/nature13681.

Scuderi, M. M., C. Collettini, and C. Marone (2017). Frictional stability and earthquake triggering during fluid pressure stimulation of an experimental fault, *Earth Planet. Sci. Lett.* **477**, 84–96, doi 10.1016/j.epsl.2017.08.009.

1070 Scuderi, M. M., E. Tinti, M. Cocco, and C. Collettini (2020). The Role of Shear Fabric in Controlling
1071 Breakdown Processes During Laboratory Slow-Slip Events, *J. Geophys. Res. Solid Earth* **125**, no. 11,
1072 e2020JB020405, doi 10.1029/2020JB020405.

1073 Shreedharan, S., Bolton, D. C., Rivière, J., & Marone, C. (2021). Competition between preslip and
1074 deviatoric stress modulates precursors for laboratory earthquakes. Earth and Planetary Science
1075 Letters, 553, 116623. https://doi.org/10.1016/j.epsl.2020.116623

1076 Stanchits, S., S. Vinciguerra, and G. Dresen (2006). Ultrasonic Velocities, Acoustic Emission
1077 Characteristics and Crack Damage of Basalt and Granite, *Pure Appl Geophys* **163**, no. 5–6, 975–994,
1078 doi 10.1007/s00024-006-0059-5.

1079 Sykes, L. R. (2021). Decadal Seismicity Prior to Great Earthquakes at Subduction Zones: Roles of
1080 Major Asperities and Low-Coupling Zones, *Int. J. Geosci.*

1081 Tchalenko, J. S. (1970). Similarities between Shear Zones of Different Magnitudes, *GSA Bull.* **81**, no.
1082 6, 1625–1640, doi 10.1130/0016-7606(1970)81[1625:SBSZOD]2.0.CO;2.

1083 Trugman, D. T. and Z. E. Ross (2019). Pervasive Foreshock Activity Across Southern California.
1084 Geophysical Research Letters 46, 8772–8781, doi 10.1029/2019GL083725

1085 Varnes, D. J. (1989). Predicting earthquakes by analyzing accelerating precursory seismic activity,
1086 *Pure Appl. Geophys.* **130**, no. 4, 661–686, doi 10.1007/BF00881603.

1087 Vavryčuk, V. (2001). Inversion for parameters of tensile earthquakes, *J Geophys Res* **106**, no. B8,
1088 16339–16355, doi 10.1029/2001JB000372.

1089 Vavryčuk, V. (2014). Iterative joint inversion for stress and fault orientations from focal mechanisms,
1090 *Geophys. J. Int.* **199**, no. 1, 69–77, doi 10.1093/gji/ggu224.

1091 Wiemer, S., and M. Wyss (2000). Minimum magnitude of completeness in earthquake catalogs:
1092 Examples from Alaska, the Western United States & Japan, *Bull Seism. Soc Am* **90**, 859–869, doi
1093 10.1785/0119990114.

1094 Wu, C., X. Meng, Z. Peng, and Y. Ben-Zion (2013). Lack of Spatiotemporal Localization of Foreshocks
1095 before the 1999 Mw 7.1 Düzce, Turkey, Earthquake, *Bull. Seismol. Soc. Am.* **104**, no. 1, 560–566, doi
1096 10.1785/0120130140.

1097 Wyss, M., C. G. Sammis, R. M. Nadeau, and S. Wiemer (2004). Fractal Dimension and b-Value on
1098 Creeping and Locked Patches of the San Andreas Fault near Parkfield, California, *Bull. Seismol. Soc.*
1099 *Am.* **94**, no. 2, 410–421, doi 10.1785/0120030054.

1100 Yamashita, F., E. Fukuyama, S. Xu, H. Kawakata, K. Mizoguchi, and S. Takizawa (2021). Two end-
1101 member earthquake preparations illuminated by foreshock activity on a meter-scale laboratory
1102 fault, *Nat. Commun.* **12**, no. 1, 4302, doi 10.1038/s41467-021-24625-4.

1103 Yoshimitsu, N., H. Kawakata, and N. Takahashi (2014). Magnitude −7 level earthquakes: A new lower
1104 limit of self-similarity in seismic scaling relationships, *Geophys. Res. Lett.* **41**, no. 13, 4495–4502, doi
1105 10.1002/2014GL060306.

1106 Zaliapin, I., and Y. Ben-Zion (2013a). Earthquake clusters in southern California I: Identification and
1107 stability, *J. Geophys. Res. Solid Earth* **118**, no. 6, 2847–2864, doi 10.1002/jgrb.50179.

1108 Zaliapin, I., and Y. Ben-Zion (2013b). Earthquake clusters in southern California II: Classification and
1109 relation to physical properties of the crust, *J. Geophys. Res. Solid Earth* **118**, no. 6, 2865–2877, doi
1110 10.1002/jgrb.50178.

1111 Zaliapin, I. and Y. Ben-Zion, 2016. A global classification and characterization of earthquake clusters,
1112 Geophys. J. Int., 207, 608–634, doi:10.1093/gji/ggw300.

1113 Zaliapin, I., A. Gabrielov, V. Keilis-Borok, and H. Wong (2008). Clustering Analysis of Seismicity and
1114 Aftershock Identification, *Phys. Rev. Lett.* **101**, no. 1, 018501, doi 10.1103/PhysRevLett.101.018501.

1115 Zang, A., F. C. Wagner, S. Stanchits, G. Dresen, R. Andresen, and M. A. Haidekker (1998). Source
1116 analysis of acoustic emissions in Aue granite cores under symmetric and asymmetric compressive
1117 loads., *Geophys J Int* **135**, no. 3, 1113–30.

1118

Figure Captions

Figure 1. Overview of mechanical data, AE activity and stick-slip processes at different temporal scales occurring during the experiment. (a,b): AE magnitudes (black dots, left axis) and axial load (red solid curve, right axis). Onsets of large (LSD), small (SSD), and confined slips events (CSD, see section 2.2 for details), the latter not reflected in geomechanical data, are marked with vertical azure lines; (b): zoom-in of the time period between 3400 s and 5000 s covering the preparatory processes ahead of the LSD1; (c,d,e): zoom-in of the time window framing the representative confined slip event CSD (c,f), small slip event SSD (d,g) and large slip event LSD (e,h) with AE magnitudes color-coded with time; (f,g,h): Corresponding top-view of the AE activity with red stars marking the location of the AE event initiating the slip. Gray area in (e) denotes short-lasting saturation of the recording system with low-frequency noise from the slip event limiting the detection of individual AE events (see text for details) following the occurrence of LSDE. Remaining time windows framing slip events are shown in Supplementary Figure S1.

Figure 2. Temporal evolution of (b) AE event rates, (c) GR *b*-value, and (d) fractal dimension (*d*-value) from a boxcounting method calculated using different moving time windows *W [s]*. For reference, the evolution of AE magnitudes and axial stress is shown in (a).

Figure 3. Temporal evolution of (a) stress and AE activity for reference, (b) Median event proximity $\hat{\eta}$ (lower $\hat{\eta}$ indicates clustering of events) and (c) proportion between AE background events (i.e. *mainshocks* and *singles*), *foreshocks* and *aftershocks* in the catalog (cf. Fig. 1) as derived from clustering analysis.

Figure 4. Temporal evolution of the (b) local fault plane variability $\widehat{\psi_f}(t)$, (c) plunge of the local maximum stress, $\delta_{\sigma 1}(t)$ (filled circles) and local stress tensor variability $\sigma_{Sij}(t)$ (dots). For reference, the evolution of AE magnitudes and axial stress is shown in (a) (cf. Fig. 1). The visible data gaps during later phases originate from the limited amount of AE-derived MTs.

Figure 5. Surface distribution of AE activity following three slip events from the phase P1 of loading (cf. Fig. 1a-b): (a): CSD T=3414 s (cf. Fig. 1c, f), (b): CSD T=3673 s, (c): SSD T=3963 s (cf. Fig. 1f, h). In (a, b, c) filled circles show AE activity within a 10-second window starting ~12 seconds following the nucleation of a slip event (star). The contour plot marks the density of events between the start of the slip event and the end of the selected time window, aggregating the damage accumulation during slip. First, two confined slips (a, b) activate small distinct patches representing cm-length-scale asperities (magenta and green regions in all subfigures). The patches mostly do not overlap suggesting a shift in activity with subsequent slips. This suggests that failing *short-scale* asperities

become inactive and ‘smooth’ at the cm-scales. The smoothed-out region expands ultimately to > 2 cm diameter (c) giving rise to a first SSD that activates a significant part of the fault surface with AE activity accumulating in a narrow diagonal region (blue region in c). The animations presenting the damage evolution framing the occurrence of three slip events are shown in Supplementary Movies S2-S4.

Table Captions

Table 1: Parameters characterizing the temporal evolution of damage and stress in the sample. Column ‘dimension sensitivity’ generalizes whether the particular parameter is sensitive to senses changes in time, space, magnitude, or their combination.

Figure 1.

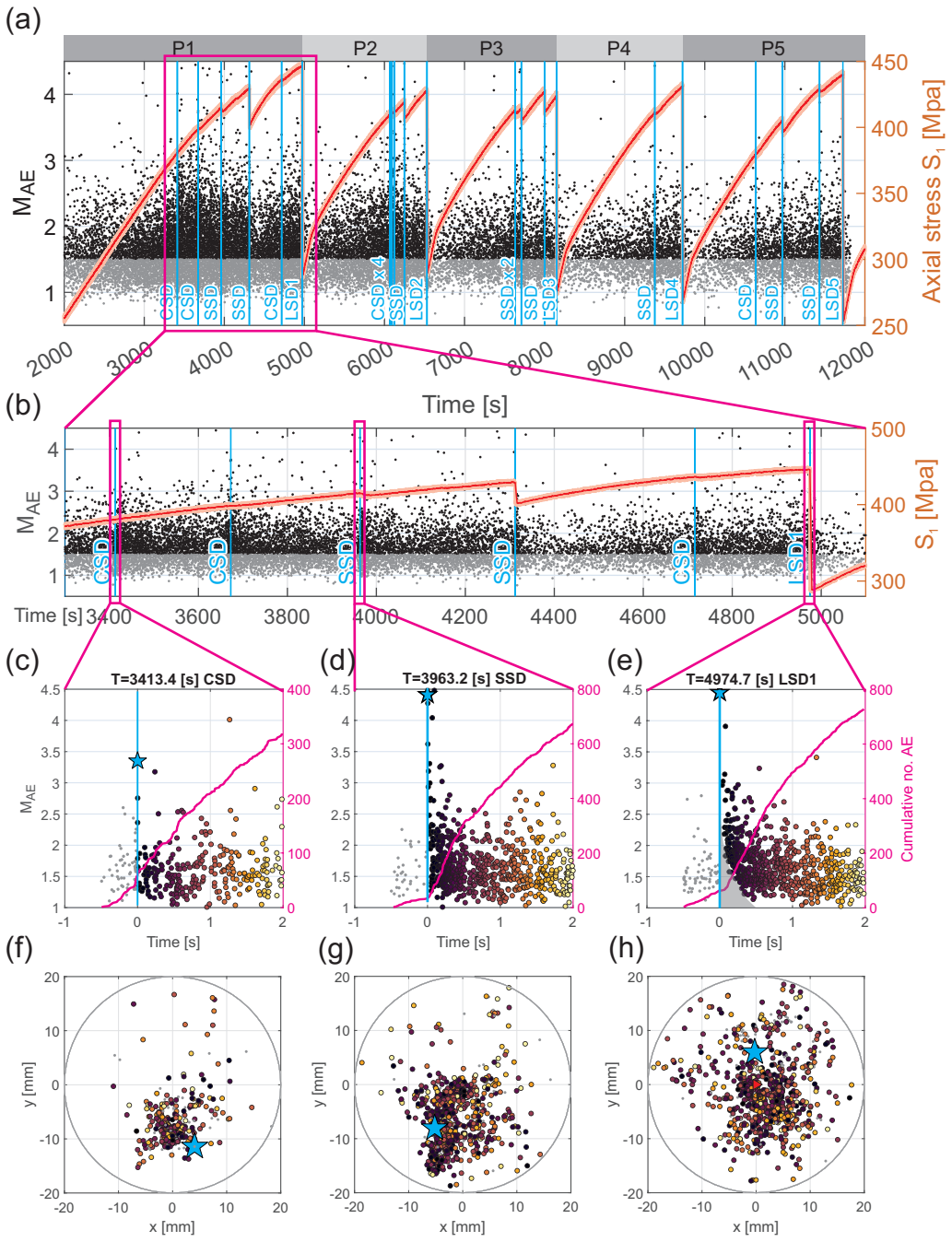
(a)
P1
P2
P3
P4
P5
M_AE
Axial stress S_1 [Mpa]
CSD
CSD
SSD
SSD
CSD
LSD1
CSD x4
SSD
LSD2
SSD x2
SSD
LSD3
SSD
LSD4
CSD
SSD
SSD
LSD5
Time [s]
(b)
M_AE
S_1 [Mpa]
CSD
CSD
SSD
SSD
CSD
LSD1
Time [s]
(c)
T=3413.4 [s] CSD
(d)
T=3963.2 [s] SSD
(e)
T=4974.7 [s] LSD1
M_AE
Cumulative no. AE
Time [s]
(f)
(g)
(h)
y [mm]
x [mm]

Figure 2.

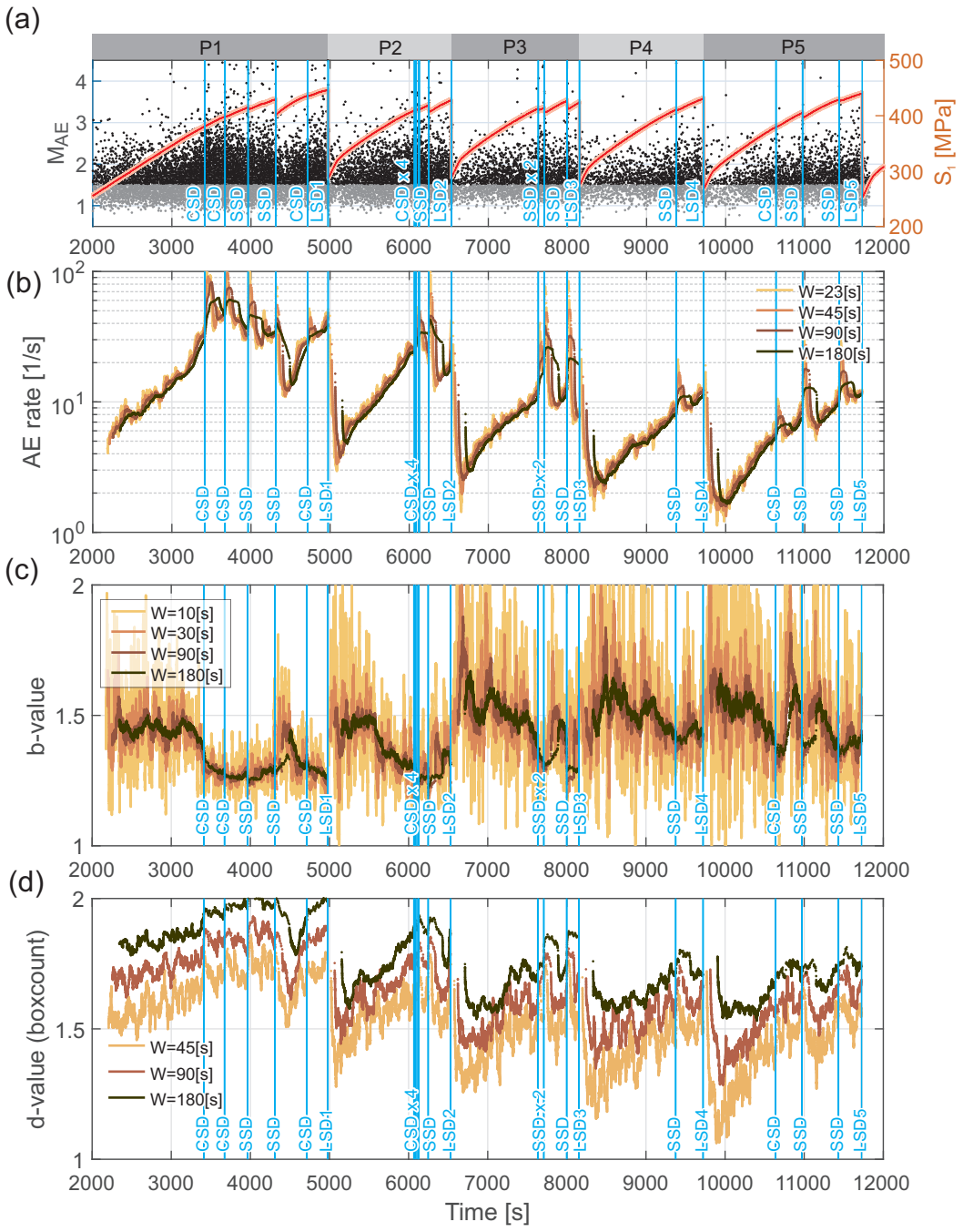
(a)
P1
P2
P3
P4
P5
M_{AE}
S, [MPa]
CSD
SSD
LSD1
CSD x 4
SSD
LSD2
SSD x 2
SSD
LSD3
SSD
LSD4
CSD
SSD
SSD
LSD5
(b)
AE rate [1/s]
W=23[s]
W=45[s]
W=90[s]
W=180[s]
(c)
b-value
W=10[s]
W=30[s]
W=90[s]
W=180[s]
(d)
d-value (boxcount)
W=45[s]
W=90[s]
W=180[s]
Time [s]

Figure 3.

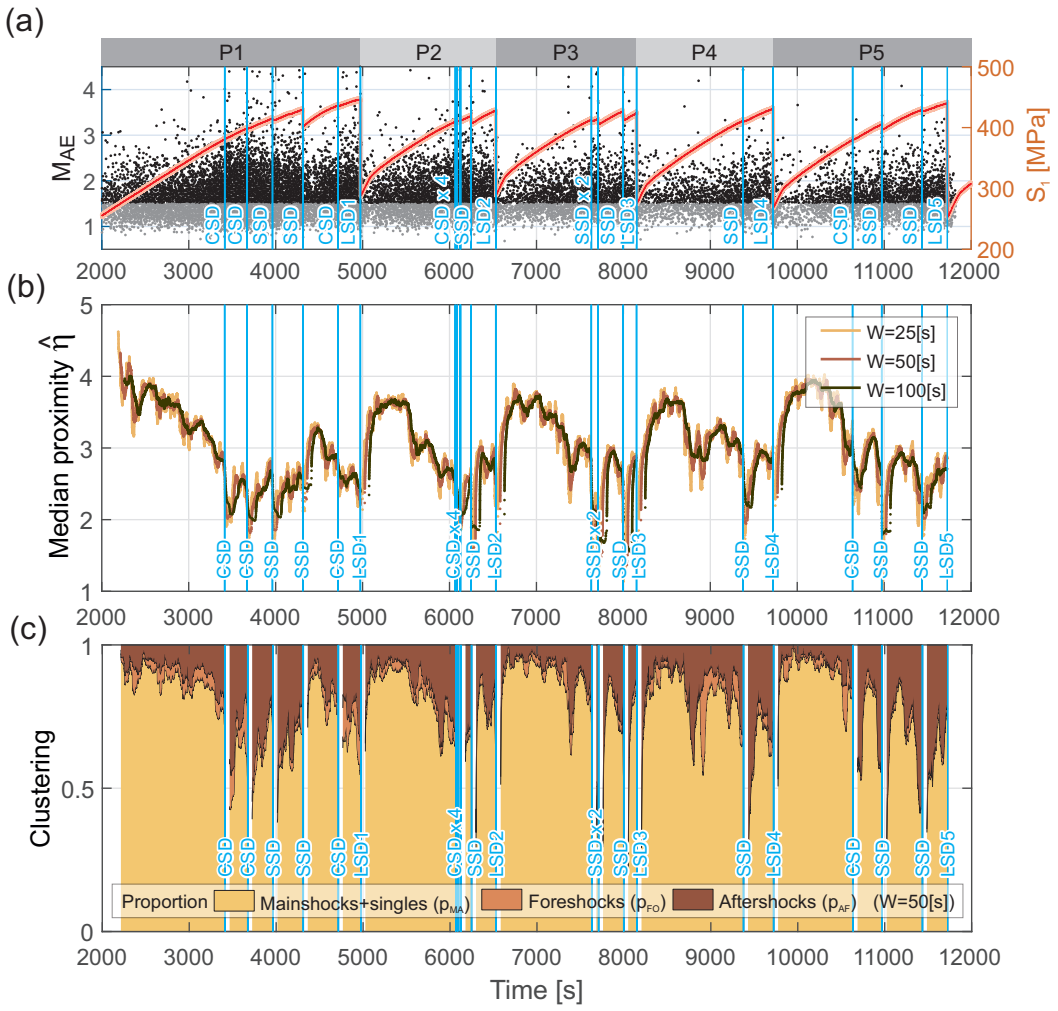
(a)
P1
P2
P3
P4
P5
M_{AE}
S_r [MPa]
CSD
SSD
LSD1
LSD2
LSD3
LSD4
LSD5
CSD x4
SSD x2
(b)
Median proximity $\hat{\eta}$
W=25[s]
W=50[s]
W=100[s]
(c)
Clustering
Proportion
Mainshocks+singles (p_{MA})
Foreshocks (p_{FO})
Aftershocks (p_{AF})
(W=50[s])
Time [s]

Figure 4.

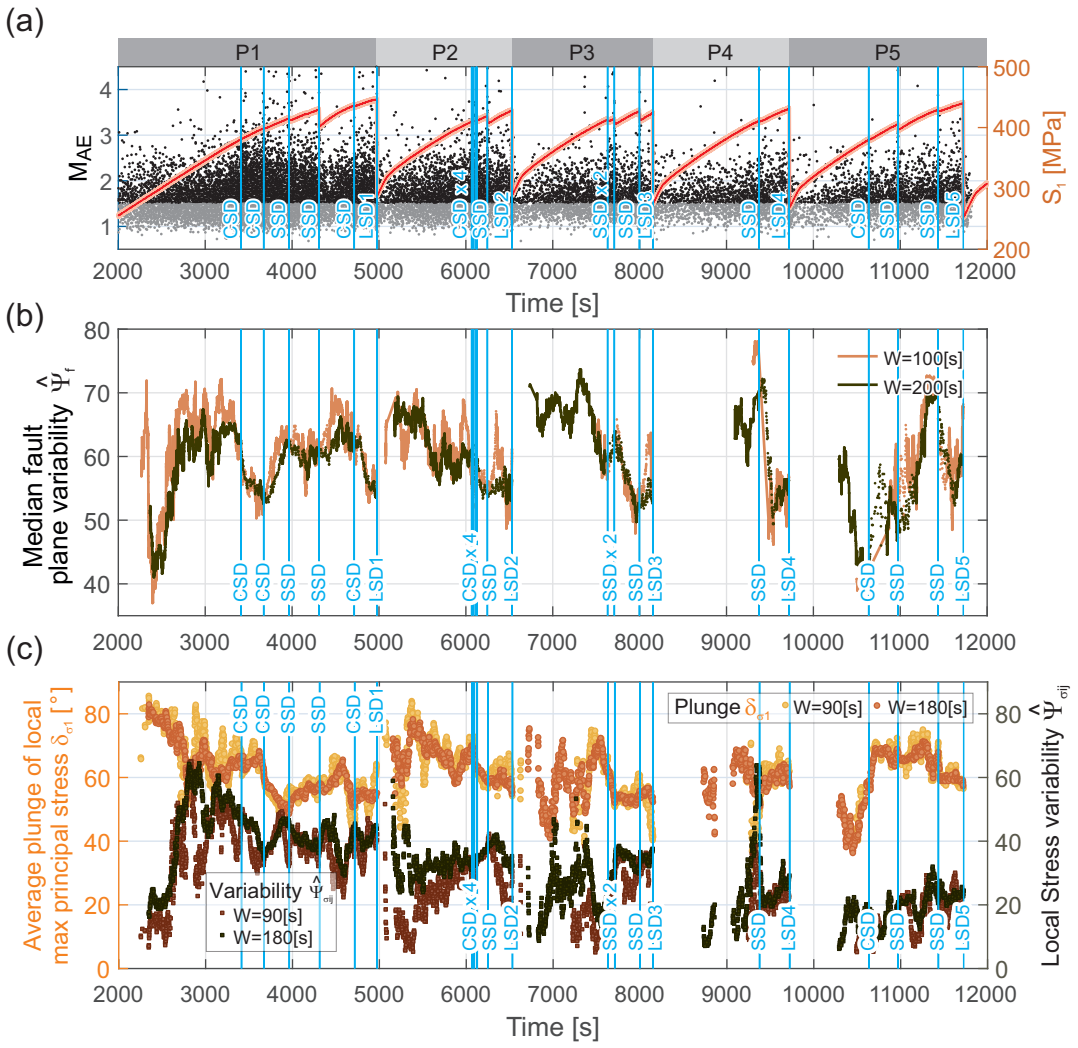
(a)
P1
P2
P3
P4
P5
M_{AE}
S_i [MPa]
CSD
SSD
LSD1
LSD2
LSD3
LSD4
LSD5
CSD x4
SSD x2
Time [s]
(b)
Median fault plane variability $\hat{\Psi}_f$
W=100[s]
W=200[s]
(c)
Average plunge of local max principal stress $\delta_{\sigma 1}$ [°]
Plunge $\delta_{\sigma 1}$
W=90[s]
W=180[s]
Variability $\hat{\Psi}_{\sigma ij}$
Local Stress variability $\hat{\Psi}_{\sigma ij}$
Time [s]

Figure 5.

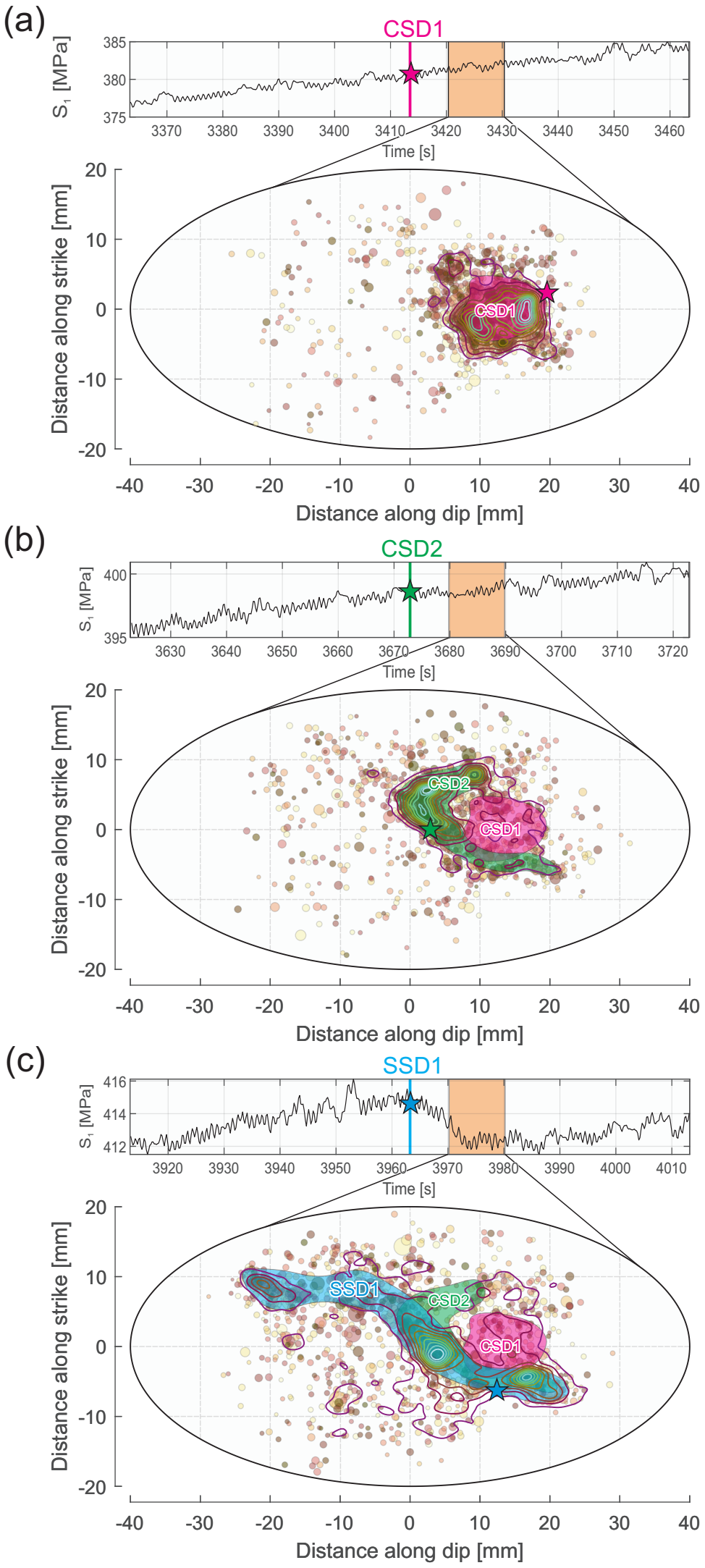
(a)
CSD1
S_1 [MPa]
Time [s]
Distance along strike [mm]
Distance along dip [mm]
(b)
CSD2
CSD1
(c)
SSD1
CSD2
CSD1

No.	Parameter	Symbol	Time windows [s]	Dimension sensitivity	Source/method
1	AE event rate	$\dot{N}$	23.5, 45, 90, 180	time	AE catalog
2	b-value (maximum likelihood)	b	10, 30, 90, 180	time-magnitude	
3	d-value (boxcounting)	d	45, 90, 180	space-time	
4	Median proximity	$\hat{\eta}$	25, 50, 100	space-time-magnitude	Clustering analysis
5	Proportion of foreshocks	p_{FO}			
6	Proportion of aftershocks	p_{AF}			
7	Proportion of mainshocks and singles	p_{MA}			
8	Median fault plane variability	$\widehat{\Psi_f}$	100, 200	space-time	Focal mechanisms
9	Plunge of local maximum principal stress	$\delta_{\sigma 1}$	90, 180	space-time	Stress tensor inversion
10	Local stress variability	$\widehat{\Psi_{\sigma ij}}$			